The Astrophysical Journal, 994:162 (16pp), 2025 December 1 https://doi.org/10.3847/1538-4357/ae0e64

Dwarf Active Galactic Nuclei from Variability for the Origins of Seeds (DAVOS): Properties of Variability-selected AGN in the Dark Energy Survey Deep Fields

Yichen Liu[1,2,3], Colin J. Burke[4], Diego Miura[4], Xin Liu[1,2,5], Qian Yang[6], Priyamvada Natarajan[4,7,8], and Charlotte A. Ward[9]

[1] Department of Astronomy, University of Illinois at Urbana-Champaign, 1002 W. Green Street, Urbana, IL 61801, USA
[2] National Center for Supercomputing Applications, University of Illinois at Urbana-Champaign, 605 East Springfield Avenue, Champaign, IL 61820, USA
[3] Steward Observatory, University of Arizona, 933 N Cherry Avenue, Tucson, AZ 85719, USA
[4] Department of Astronomy, Yale University, 219 Prospect Street, New Haven, CT 06511, USA; colin.j.burke@yale.edu
[5] Center for Artificial Intelligence Innovation, University of Illinois at Urbana-Champaign, 1205 West Clark Street, Urbana, IL 61801, USA
[6] Center for Astrophysics | Harvard & Smithsonian, 60 Garden Street, Cambridge, MA 02138, USA
[7] Department of Physics, Yale University, 217 Prospect Street, New Haven, CT 06520, USA
[8] Black Hole Initiative, Harvard University, 20 Garden Street, Cambridge, MA 02138, USA
[9] Department of Astrophysical Sciences, Princeton University, Princeton, NJ 08544, USA

Received 2025 March 7; revised 2025 September 1; accepted 2025 September 23; published 2025 November 24

Abstract

We study the black hole mass–host galaxy stellar mass relation, $M_{\rm BH}$–M_*, for a sample of 706 $z \lesssim 1.5$ and $i \lesssim 24$ optically variable active galactic nuclei (AGNs) in three Dark Energy Survey (DES) Deep Fields: C3, X3, E2, which partially cover Chandra Deep Field-South, XMM Large Scale Structure survey, and European Large Area ISO Survey, respectively. The parent sample was identified by optical variability from the DES supernova survey program imaging. Using publicly available spectra and photometric catalogs, we consolidate their spectroscopic redshifts, estimate their black hole masses using broad line widths and luminosities, and obtain improved stellar masses using spectral energy distribution fitting from X-ray to mid-infrared wavelengths. Our results confirm previous work from Hyper-Suprime Camera imaging that variability searches with deep, high-precision photometry can reliably identify AGNs in low-mass galaxies up to $z \sim 1$. However, we find that the hosted black holes are more massive than predicted by the local AGN relation, fixing host galaxy stellar mass. Instead, $z \sim 0.1$–1.5 variability-selected AGNs lie in between the $M_{\rm BH}$–M_* relation for local inactive early-type galaxies and local active galaxies. This result agrees with most previous studies of the $M_{\rm BH}$–M_* relation for AGNs at similar redshifts, regardless of the selection technique. We demonstrate that studies of variability-selected AGN provide critical insights into the low-mass end of the $M_{\rm BH}$–M_* relation, shedding light on the occupation fraction of that provides constraints on early black hole seeding mechanisms and self-regulated feedback processes during their growth and coevolution with their hosts.

Unified Astronomy Thesaurus concepts: Active galaxies (17); Dwarf galaxies (416); Surveys (1671); Black holes (162); Galaxy nuclei (609); Active galactic nuclei (16)

Materials only available in the online version of record: machine-readable table

1. Introduction

Local scaling relations between supermassive black hole (SMBH) mass $M_{\rm BH}$ and their host galaxy properties (e.g., total galaxy stellar mass, bulge stellar mass, stellar velocity dispersion, bulge luminosity: $M_{\rm BH}$–M_*, $M_{\rm BH}$–$M_{*,\rm bulge}$ $M_{\rm BH}$–σ_*, $M_{\rm BH}$–$L_{*,\rm bulge}$) in both active and inactive galaxies are key to our understanding of SMBH-host galaxy coevolution (e.g., M. G. Haehnelt et al. 1998; J. Magorrian et al. 1998; J. Kormendy & L. C. Ho 2013; A. E. Reines & M. Volonteri 2015). These empirical scaling relations are widely taken as evidence for some form of self-regulated feedback between black hole accretion and star formation in active galactic nuclei (AGNs). However, there is no consensus model of how AGN feedback operates (e.g., A. C. Fabian 2012). Observational measures of the SMBH–host scaling relations over a wide range of redshifts and luminosities are critical for placing new constraints on such models (e.g., A. Ricarte & P. Natarajan 2018). In addition to informing theoretical models of AGN feedback, the low-mass end of the SMBH–host scaling relations may be sensitive to the initial mass function of high-redshift SMBH seeds and their subsequent growth modes (M. Volonteri & P. Natarajan 2009; P. Natarajan 2011).

While the existence of an $M_{\rm BH}$–σ_* relation may be a universal feature of structure formation (e.g., R. C. E. van den Bosch 2016), the slope and normalization of the local $M_{\rm BH}$–M_* scaling relations differ significantly for actively accreting AGNs and galaxies hosting inactive black holes (A. E. Reines & M. Volonteri 2015). The SMBH–host galaxy scaling relations have been studied in AGNs selected over a range of wavelengths and redshifts (e.g., S. J. Lilly et al. 2007; A. Merloni et al. 2010; F. Civano et al. 2016; H. Suh et al. 2020; X. Ding et al. 2020; J. I. H. Li et al. 2021, 2023; M.-Y. Zhuang et al. 2024; M. Mezcua et al. 2023, 2024). In our previous work, we studied $z < 4$ variability-selected AGNs from the Hyper Suprime-Cam Subaru Strategic Program (HSC-SSP; Y. Kimura et al. 2020) in the COSMOS field and their $M_{\rm BH}$–M_* scaling relation (C. J. Burke et al. 2024b). These results generally confirm that these intermediate and higher redshift AGNs have overmassive black holes compared to the local ($z < 0.055$) AGN relation of $M_{\rm BH}/M_* \sim 0.025\%$ (A. E. Reines & M. Volonteri 2015), regardless of the selection method. Instead, nonlocal AGNs appear to follow the $M_{\rm BH}$–M_* relation more closely for local inactive galaxies.

Meanwhile, James Webb Space Telescope (JWST) $z \sim 4$–7 AGNs have black hole masses ∼10–100 times more massive compared to local AGNs with comparable stellar mass hosts (Y. Harikane et al. 2023; D. D. Kocevski et al. 2023; R. Maiolino et al. 2024; H. Übler et al. 2023). Recently, V. Kokorev et al. (2023) identified a $z = 8.5$ AGN with an $M_{\rm BH}/M_*$ ratio of at least ∼30%, and Á. Bogdán et al. (2023), P. Natarajan et al. (2024), and A. D. Goulding et al. (2023) reported a $z \approx 10.1$ quasar UHZ1 and the source GHZ9 at $z \approx 10.4$ (O. E. Kovács et al. 2024), both with $M_{\rm BH}/M_* \sim 1$. The $z = 10.6$ source GN-z11 also lies above the $M_{\rm BH}$–M_* for local AGNs (R. Maiolino et al. 2024). Elevated $M_{\rm BH}/M_*$ ratios at redshifts of $9 < z < 12$ are a predicted outcome of heavy black hole seed formation in the early Universe via direct collapse of pristine gas (P. Natarajan et al. 2017). On the other hand, J. Li et al. (2025) identified a population of $z \sim 3$–5 AGNs with $M_{\rm BH}/M_*$ ratios that are more in-line with the relation for local inactive galaxies than these earlier JWST results (but still more massive than the A. E. Reines & M. Volonteri (2015) relation for local AGNs), which is consistent with the AGN sample of Y. Sun et al. (2024) selected from the JADES result at a lower redshift of $1 \lesssim z \lesssim 4$.

An important caveat is that these observations are strongly affected by selection biases. For example, AGNs selected by luminosity can produce a false redshift evolution in the host galaxy scaling relations (T. R. Lauer et al. 2007). Statistical modeling by J. Li et al. (2025) shows how a combination of selection biases and measurement uncertainties can result in elevated $M_{\rm BH}/M_*$ ratios for $z > 6$ JWST AGNs. Furthermore, uncertainties from single-epoch virial black hole mass measurements can lead to the systematic overestimation of black hole masses, especially at the high mass end of these relations (Y. Shen & B. C. Kelly 2010). Therefore, it is imperative to select AGNs with lower masses and luminosities over a wide range of redshifts to mitigate these selection biases (e.g., T. Izumi et al. 2019, 2021; H. Suh et al. 2020).

Optical variability is uniquely suited to uncover faint, low-mass AGNs in dwarf galaxies, which are otherwise missed by traditional selection methods (C. Villforth et al. 2012; V. F. Baldassare et al. 2018, 2020; G. Halevi et al. 2019; C. J. Burke et al. 2020, 2022, 2023; H. Guo et al. 2020; C. Ward et al. 2022). In this paper, we obtain black hole masses, redshifts, and robust stellar masses for variability-selected low-mass AGNs from C. J. Burke et al. (2022). These sources were identified from light curves from the Dark Energy Survey supernova (DES-SN) program (M. Vincenzi et al. 2024), a subset of the wide-field DES (Dark Energy Survey Collaboration et al. 2016). About 31% of the sources are detected in the X-ray. Using these data, we measure the $M_{\rm BH}$–M_* relation at $z \sim 0.1$–1.5. Our sample has a bolometric luminosity range of $L_{\rm bol} \sim 10^{44-46}$ erg s^{-1}, comparable to the COSMOS X-ray selected sample of H. Suh et al. (2020). In combination with previous work (C. J. Burke et al. 2024b), we find that this sample of $z \sim 0.1$–3.5 variability-selected AGNs has overmassive black holes compared to the local AGN relation of A. E. Reines & M. Volonteri (2015), broadly consistent with most previous studies of AGNs at similar median redshifts ($z \sim 0.5$–1) selected with other techniques (A. Merloni et al. 2010; J. I. H. Li et al. 2021; M. Mezcua et al. 2023; G. Mountrichas 2023; M. A. Stone et al. 2024; Y. Zhang et al. 2023; M.-Y. Zhuang et al. 2024; T. S. Tanaka et al. 2025).

This paper is organized as follows. In Section 2, we describe our procedure for collating archival spectra and photometry and constructing a spectroscopic redshift database for our variable AGN sample. In Section 3, we describe our procedure for estimating the stellar masses of the host galaxies by fitting the spectral energy distributions (SEDs) to the broadband photometry of the host galaxy in the presence of an AGN. In Section 4, we describe our black hole mass estimates derived from fitting the broad lines in the spectra. In Section 5, we place these sources on the $M_{\rm BH}$–M_* relation and compare our results with previous work. We discuss our results in Section 6 and their implications in Section 7.

1.1. DES Deep Field Data

In this work, we use the sample of variable AGNs selected by C. J. Burke et al. (2022) from g-band light curves from the DES-SN program. Both resolved and unresolved sources were selected, using difference imaging for resolved sources that tend to be at lower redshifts.[10] DES-SN observed 10 fields over 6 yr with a cadence of about 7 days (with seasonal gaps) in the $griz$ bands during the observing. The DES-SN observations generally took place when the seeing was poor. The median g-band seeing was $\sim 1\farcs2$ (J. Lee et al. 2023). The single-epoch photometric precision is $g \sim 24.5$ (limiting point-spread function magnitude where the detection efficiency drops to 50% R. Kessler et al. 2015). These fields have been continuously observed since then (M.-Y. Zhuang et al. 2024) and will be part of the upcoming Legacy Survey of Space and Time (LSST) using the Vera C. Rubin Observatory (Ž. Ivezić et al. 2019).

Our parent sample is restricted to three DES-SN fields with eight-band ($ugrizJHK_S$) deblended, stacked model-based photometry (W. G. Hartley et al. 2022) to a uniform depth of $i = 25$, which is critical to obtaining stellar mass estimates. These fields overlap with the Chandra Deep Field-South (CDF-S; B. Luo et al. 2017), the XMM Large Scale Structure survey fields (O. Garcet et al. 2007), and the European Large Area ISO Survey (S. Oliver et al. 2000). The deep fields of our parent sample of AGNs from C. J. Burke et al. (2022) are denoted C3, X3, and E2, respectively. The total C3+X3+E2 area with optical + near-infrared (NIR) photometry is ∼4.6 deg^2. The COSMOS field was also observed by DES, but at a more uneven cadence, and was therefore not included in the C. J. Burke et al. (2022) selection. The COSMOS plus DES-SN fields are collectively known as the DES Deep Fields.

1.2. The DAVOS Deep Field Variable AGN Sample

We refer to our parent sample of 706 sources in this work from C. J. Burke et al. (2022) as the DES-SN variable AGN sample. Later, we will supplement this sample with 491 variable AGNs selected from the HSC-SSP in the COSMOS field by Y. Kimura et al. (2020) using the results presented in C. J. Burke et al. (2024b). In total, we have 1197 DAVOS variable AGNs in these deep fields. In this work, we aim to

---

[10] These light curves were recomputed using a single template for all observing seasons, which differs from the DES-SN difference imaging light curves used for the transient search pipeline (R. Kessler et al. 2015).

Table 1
List of Sources of the Optical/NIR Spectroscopic Redshifts for the DES-SN AGNs

Count	References	Name
50	M. L. Menzel et al. (2016)	SDSS and WISE AGN
44	C. J. Burke et al. (2022)	OzDES[a]
28	S. S. Tie et al. (2017)	WISE and DES AGN
16	M. Y. Mao et al. (2012)	ATLAS
13	J. D. Silverman et al. (2010)	CDF-S Faint X-ray
12	R. Ahumada et al. (2020)	SDSS DR16
6	S. Alam et al. (2015)	SDSS-III DR12
6	N. Sacchi et al. (2009)	Spitzer/SWIRE
5	I. K. Baldry et al. (2018)	GAMA DR3
3	F. Zou et al. (2023)	XMM-SERVS
3	I. Pâris et al. (2018)	SDSS DR14Q
3	B. Garilli et al. (2014)	VIPERS PDR-1
3	C. J. Burke et al. (2022)	PanS[a]
3	C. J. Burke et al. (2022)	ACES[a]
2	C. Cheng et al. (2021)	Low-z faint galaxies
2	M. Scodeggio et al. (2018)	VIPERS PDR-2
2	H. Suh et al. (2015)	FMOS AGN
2	M. C. Cooper et al. (2012)	ACES
2	S. Eales et al. (2009)	BLAST
2	C. J. Burke et al. (2022)	SDSS[a]
1	B. W. Lyke et al. (2020)	SDSS DR16Q v4
1	M. Lacy et al. (2013)	Spitzer AGN
1	O. Le Fèvre et al. (2013)	VVDS
1	A. Hernán-Caballero & E. Hatziminaoglou (2011)	Spitzer
1	L. Xia et al. (2011)	Magellan LDSS-3
1	C. J. Burke et al. (2022)	VVDS[a]
1	C. J. Burke et al. (2022)	SNLS[a]
1	C. J. Burke et al. (2022)	GAMA[a]
1	C. J. Burke et al. (2022)	2dFG[a]

Note.
[a] Data remain unchanged from C. J. Burke et al. (2022).

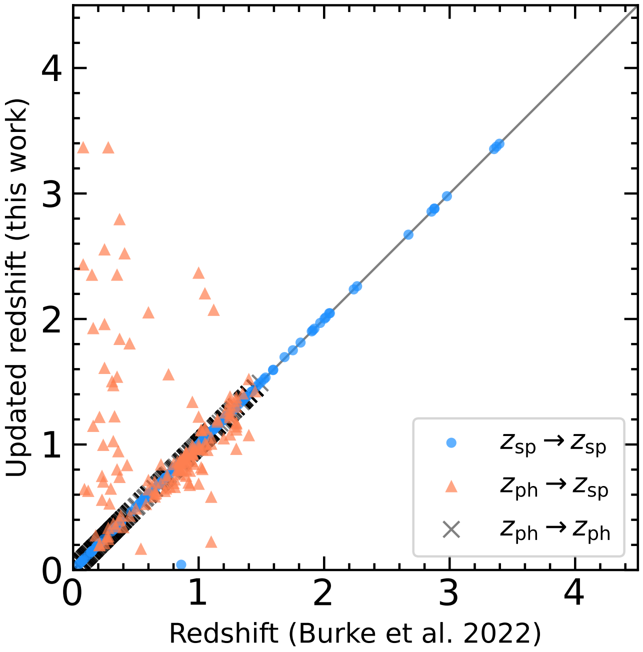

Figure 1. Updated redshifts in this work from SIMBAD, OzDES, and DESI vs. original redshifts from C. J. Burke et al. (2022). The redshifts updated from photometric to spectroscopic are labeled using orange triangle symbols, and the unchanged or updated photometric and spectroscopic redshifts are shown as gray crosses and blue dots, respectively. A number of previous catastrophically underestimated photometric redshifts have been updated

estimate the black hole and host galaxy stellar masses for the DES-SN variable AGN sample. We also eliminate variable star contaminates from these parent samples, such as cataclysmic variable stars in the Milky Way halo.

2. Data Analysis

2.1. Spectra Database

C. J. Burke et al. (2022) and W. G. Hartley et al. (2022) compiled 146 spectroscopic redshifts in the DES Deep Fields, which we supplement here using the SIMBAD database (M. Wenger et al. 2000), the Australian Dark Energy Survey (OzDES) spectroscopy from their second data release, and Dark Energy Spectroscopic Instrument (DESI) spectroscopy from data release 1. We identified additional spectroscopic redshifts from the literature that were indexed at the time of writing by SIMBAD using an ASTROQUERY (A. Ginsburg et al. 2019) SIMBAD search. The SIMBAD redshifts originate from a variety of individual spectroscopic surveys and follow-up programs (see references in Table 1). We restricted our SIMBAD search to good quality spectroscopic redshifts from optical or NIR spectra using the flags RVZ_WAVELENGTH = =‘O′ or RVZ_WAVELENGTH = =‘N′ and rvz_qual! = ‘E′. The first two constraints restrict the search to redshifts from optical/NIR spectra. The last constraint excludes photometric redshifts. Out of 706 AGN candidates, we removed 10 spectroscopically classified variable stars (ID = 14, 84, 327, 328, 426, 544, 626, 673, 669, and 680) from our parent sample using the OTYPE key. ID = 426 is a spectroscopically confirmed RR Lyrae variable star, and ID = 669 is a spectroscopically confirmed cataclysmic variable star. Finally, we downloaded the publicly available spectra from these sources (see Appendix A). We also obtained spectroscopic redshifts from the DESI Early Data Release (DESI Collaboration et al. 2024), which have not yet been indexed by SIMBAD at the time of writing. We assign fiducial spectroscopic redshifts according to the following priority: DESI (5 sources) > OzDES (147 sources) > SIMBAD (99 sources). For example, when both DESI and SIMBAD have redshifts, we adopt DESI’s one.

If no spectroscopic redshift was found, we use the photometric redshifts from C. J. Burke et al. (2022) (407 sources; Section 2.2). Our updated redshifts are shown in Figure 1. The bolometric luminosity and redshift distributions are shown in Figure 2. A table showing the sources of the public spectroscopic redshifts for the DES-SN variable AGNs is shown in Table 1. We found no inconsistent spectroscopic redshifts between our adopted spectroscopic redshifts in this work and the spectroscopic redshifts of C. J. Burke et al. (2022). To include cases where a single source has more than one available spectrum from different programs, we always repeat the matching between the DES-SN variable AGNs and the spectroscopic sample when downloading the spectra from publicly available sources.

2.2. Photometric Redshifts

For sources without a reliable spectroscopic redshift, we use the photometric redshifts from C. J. Burke et al. (2022) derived from the Skew-t method of Q. Yang et al. (2017). This

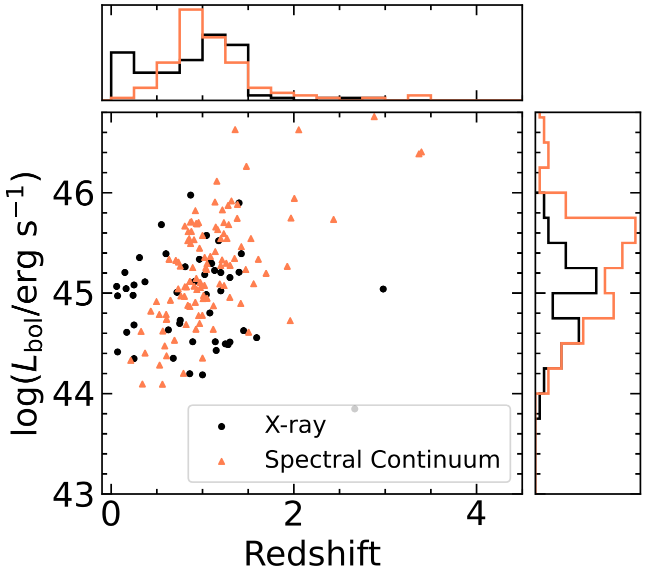

Figure 2. The bolometric AGN luminosity, estimated as 10 times the 2–10 keV X-ray luminosity (following F. Duras et al. 2020), is plotted against our updated redshifts. The distributions of redshift and bolometric luminosity are displayed in the upper and right panels, respectively.

approach uses the asymmetries in the relative flux distributions as a function of redshift and magnitude and was trained on a sample of AGNs and galaxies. Using our newly compiled spectroscopic redshifts as our ground truth, we estimate the scatter in the photometric redshifts following C. J. Burke et al. (2024b) as $\sigma = 1.4826$ MAD, where MAD is the median absolute deviation, which is robust to outliers. We find $\sigma = 0.62$ for the entire data set, but $\sigma = 0.17$ at spectroscopic redshifts of <1.5. This indicates a large outlier fraction due to contamination from high-redshift quasars. A comparison between the photometric redshifts and our updated spectroscopic redshifts for the DES-SN AGNs is shown in Figure 3.

3. SED Fitting

We recomputed the stellar masses for the C. J. Burke et al. (2022) DES-SN variable AGNs using our newly compiled spectroscopic redshifts. We use the $ugrizJHK_S$ deblended, stacked model-based photometry from W. G. Hartley et al. (2022), which is publicly available. The photometry is derived from DES imaging along with supplemental u-band DECam imaging that was obtained in these fields. The JHK_S imaging of E2, C3, and X3 is from the VIDEO survey (M. J. Jarvis et al. 2013). We also extended the photometry to UV and IR by matching the C. J. Burke et al. (2022) DES-SN variable AGNs to the Revised Catalog of GALEX UV Sources (L. Bianchi et al. 2017) and Spitzer Enhanced Imaging Products Source (SEIP) List (Spitzer Science Center & Infrared Science Archive 2021), respectively. For SEIP, we use all matched Spitzer data and associated ALLWISE data with quality flags of either A, B, or C. In addition, the X-ray 2−7 keV photometry is from version 2.0 of the Chandra Source Catalog (I. N. Evans et al. 2010), and the X-ray 0.2−12 keV photometry is from the XMM-Newton serendipitous survey (N. A. Webb et al. 2020). We converted X-ray fluxes from erg $\rm s^{-1}\,cm^{-2}$ to mJy using the method provided by G. Yang et al. (2020). All catalogs are matched within 1″. The inclusion of the optical to mid-infrared photometry is essential to constrain the star formation and reprocessed dust emission. Additionally, including the X-ray photometry helps constrain the contribution from AGN emission (G. Yang et al. 2020). This multiwavelength SED helps to eliminate some degeneracies between star formation and AGN emission, which can lead to spurious stellar mass estimates (e.g., C. J. Burke et al. 2024b).

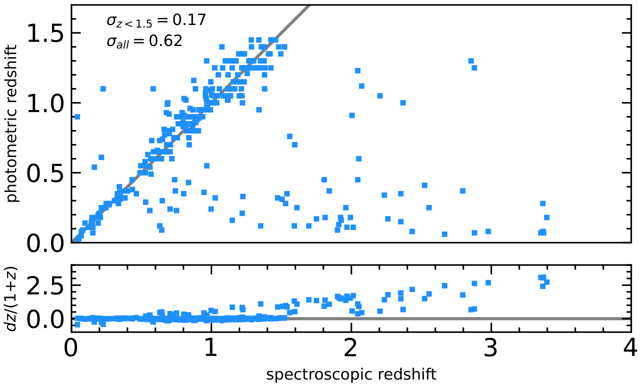

Figure 3. Comparison of the photometric redshifts from C. J. Burke et al. (2022) and the spectroscopic redshifts obtained in this work. The photometric redshifts are determined using the approach outlined in Q. Yang et al. (2017). The root mean square error values of all the sources and $z_{\rm spec} < 1.5$ sources are displayed in the upper left corner of the figure panel. A gray $y = x$ line is included for reference.

We use version 2022.1 of the CIGALE code (D. Burgarella et al. 2005; S. Noll et al. 2009; M. Boquien et al. 2019; G. Yang et al. 2020, 2022) for SED fitting. This version includes X-ray fitting modules from X-CIGALE and incorporates detailed AGN emission models that have been thoroughly tested on both galaxies and AGNs (G. Yang et al. 2020, 2022). The codes enforce a self-consistent energy balance between different emission and absorption processes across the electromagnetic spectrum. A large set of models is involved and fitted to the data, enabling the estimation of stellar mass, star formation rate (SFR), and AGN contribution through a Bayesian-like analysis of the likelihood distribution.

We adopt a delayed exponential star formation history, varying the e-folding time and the age of the stellar population while assuming solar metallicity. However, systematic uncertainties arise from different choices of initial mass function, stellar population models, and star formation histories. F. Zou et al. (2022) found that variations in parametric star formation histories lead to systematic stellar mass differences of about 0.1 dex for AGNs in the redshift range of $z = 0$–6. The total systematic errors on stellar masses from these assumptions are typically ∼0.2–0.3 dex (C. Conroy 2013).

For our analysis, we use the widely adopted G. Chabrier (2003) initial stellar mass function, along with the stellar population models from G. Bruzual & S. Charlot (2003) and the nebular emission template of A. K. Inoue (2011). Dust extinction is modeled using the C. Leitherer et al. (2002) extension of the D. Calzetti et al. (2000) attenuation law, while dust emission follows the B. T. Draine et al. (2014) updates to the B. T. Draine & A. Li (2007) model. For AGN emission, we apply the SKIRTOR clumpy two-phase torus model (M. Stalevski et al. 2012, 2016), incorporating additional polar extinction for the UV-IR AGN SED. The X-ray AGN emission is modeled with the $\alpha_{ox} - L_{2500\,A}$ relation (e.g., A. T. Steffen et al. 2006; D. W. Just et al. 2007).

We assume a Type 1-like inclination angle of 30° for our optically variable AGNs. This choice is supported by prior

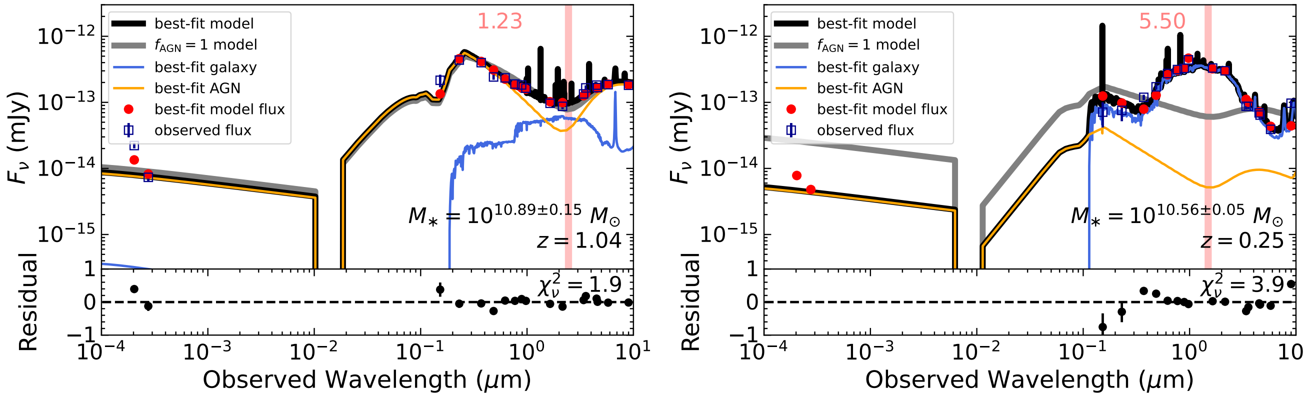

Figure 4. Left panel: an example SED-fitting result for an AGN-dominated source (C. J. Burke et al. (2022) ID = 43). In this case, including a stellar emission component does not significantly improve the fit, meaning that the stellar emission and related parameters, such as stellar mass and star formation history, cannot be reliably constrained. Right panel: an example SED-fitting result for a source that is not AGN dominated (C. J. Burke et al. (2022) ID = 265). Here, adding a stellar emission component improves the best-fit χ^2_ν, and the resulting best-fit stellar emission shows a significant excess over the AGN continuum emission near ∼1.2 μm, allowing for a reliable stellar mass estimate. The uncertainties on the stellar mass are statistical only, as provided by CIGALE. The vertical red line near 1.2 μm marks the region where AGN emission is at a minimum. The red number is the monochromatic flux ratio of the star formation emission component (blue) in the best-fit model SF+AGN model and the total AGN-dominated model (gray). Both redshifts are spectroscopic.

studies, which indicate that different viewing angles are largely degenerate with the typical values of 30° and 70° for Type 1 and Type 2 AGNs, respectively (e.g., G. Mountrichas et al. 2021; A. F. Ramos Padilla et al. 2022). Table 2 of C. J. Burke et al. (2024b) lists the CIGALE input parameters, with example SED-fitting results presented in Figure 4. The derived stellar masses range from $M_* \sim 10^{7-11.5}\ M_\odot$.

3.1. Reliability of Stellar Mass Estimates

For galaxies with significant AGN emission, accurately modeling star formation and deriving reliable stellar masses requires constraining or subtracting the AGN contribution. This is particularly challenging because the UV/optical emission from an unobscured AGN accretion disk can be highly degenerate with stellar light. When the SED is AGN dominated, the stellar component becomes overwhelmed, making it difficult to constrain stellar mass and star formation history (e.g., A. Merloni et al. 2010; L. Ciesla et al. 2015). Robust stellar mass estimates often require high-resolution optical/NIR imaging with source profile fitting to remove the AGN point source, or spectral AGN templates fit to the continuum and emission lines and scaled to the photometry (A. E. Reines & M. Volonteri 2015). In the absence of high-resolution data, broadband SED fitting can be used with certain limitations. To assess whether stellar emission—and thus stellar mass—can be constrained from SED fitting, we apply a model comparison method following C. J. Burke et al. (2024b).

This approach involves first fitting the SED using an AGN-dominated model, setting the AGN fraction to $f_{\rm AGN} = 0.9999$, where $f_{\rm AGN}$ represents the AGN contribution in the observed-frame 0.5–1 μm range. This ensures that the SED is fully dominated by AGN emission when the $f_{\rm AGN} \sim 1$, as AGN contribution is minimal at all wavelengths. Due to technical constraints in CIGALE (G. Yang et al. 2020), $f_{\rm AGN}$ cannot be set exactly to unity, so we round it to 1 for clarity in the rest of this paper. Next, we refit the SED using a mixed AGN+stellar emission model, allowing $f_{\rm AGN}$ to vary between 0 and 1 in the observed-frame 0.1–0.3 μm range, where most of our spectra exhibit significant AGN continuum emission. Since our sources are identified based on optical light curves, AGN emission is expected to be prominent in this range. Indeed, most of our spectra show significant AGN continuum emission at these wavelengths because the sources have been identified from optical band light curves.

We consider stellar masses to be reliable only for SEDs that show significant stellar emission at rest-frame 1.2 μm, which cannot be reproduced by a fully AGN-dominated model. To quantify this, we compute the ratio of the total model fit from the AGN+stellar model to that of the AGN-dominated model. A stellar mass is deemed reliable if this ratio exceeds 1.2 (C. J. Burke et al. 2024b). This method is similar to some previous approaches (A. Merloni et al. 2010; H. Suh et al. 2020; C. J. Burke et al. 2022) and effectively removes SEDs that are degenerate with AGN emission at rest-frame 1.2 μm, where AGN contamination is minimized.

Our approach improves upon previous stellar mass estimates in C. J. Burke et al. (2022) by incorporating X-ray data, which significantly constrains the AGN contribution to the SED (C. J. Burke et al. 2022; G. Yang et al. 2022). Additionally, comparing reduced χ^2 values alone, as done in C. J. Burke et al. (2022), is less reliable because χ^2 depends on photometric uncertainties, and model parameter choices (e.g., overfitting stellar emission), and does not always indicate a better fit in the optical-NIR region, where stellar emission is strongest and stellar masses are derived (C. J. Burke et al. 2022). A detailed comparison between the two approaches is presented in Appendix C.

Figure 4 presents example SEDs with both reliable and unreliable stellar mass estimates, reported from the AGN+stellar emission model. The scatter in the derived stellar masses is typically around 0.2 dex, an uncertainty not fully accounted for in CIGALE, which tends to underestimate stellar mass uncertainties. To compensate, we add 0.2 dex in quadrature to the CIGALE uncertainties in all figures throughout this paper. We adopt the “Bayesian-like” parameter estimates and uncertainties from CIGALE, which are derived by weighting each model solution by $\exp(-\chi^2/2)$ (M. Boquien et al. 2019), with final values obtained from the likelihood-weighted mean and standard deviation.

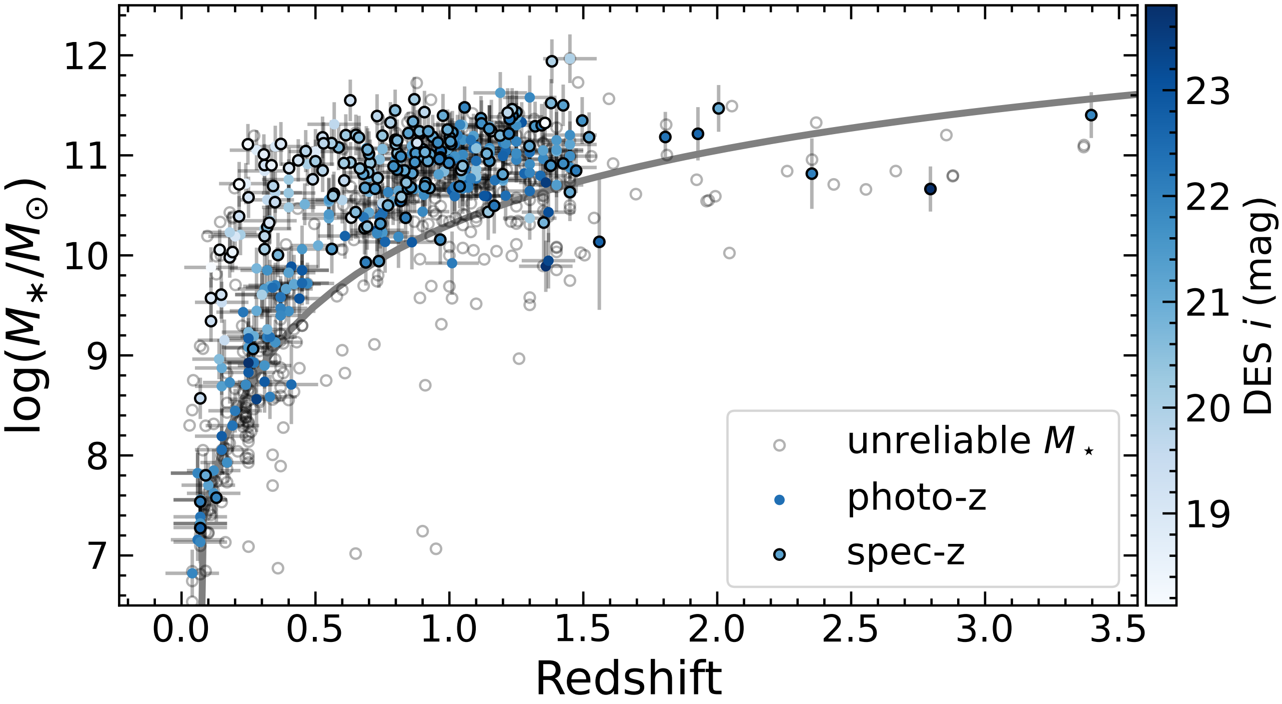

Figure 5. Host galaxy stellar mass vs. redshift for DES-SN variable AGNs with stellar mass estimates from broadband SED fitting using CIGALE. Gray circles: unreliable stellar mass ($\chi^2_\nu > 5$ or star formation excess <1.2). Colored circle symbols with black border: reliable stellar mass calculated from spectroscopic redshift. Colored circle symbols without a black border: reliable stellar mass calculated from the photometric redshift. Gray curve: theoretical detection limit.

3.2. Detection Limits

Figure 5 presents our derived stellar mass estimates versus redshift for the DES-SN AGNs. The gray curves represent the theoretically predicted stellar mass detection limits, following C. J. Burke et al. (2023). These stellar mass horizon curves are calculated by assuming a limiting detectable variability amplitude of 0.1 mag and incorporating the modified correlations between optical variability amplitude and mass (e.g., C. L. MacLeod et al. 2010; K. L. Suberlak et al. 2021), as described in C. J. Burke et al. (2023). The predicted detection limits are based on a typical variability amplitude of 0.1 mag and a photometric precision from Ž. Ivezić et al. (2019), with a DES single-epoch limiting magnitude of $g = 24.5$ (C. J. Burke et al. 2022).

4. Spectral Measurements

4.1. Publicly Available Spectroscopic Data

We obtained publicly available spectra for our parent sample of DES Deep Field AGNs from Table 1. The list of downloaded spectra differs slightly from our spectroscopic redshift database in Table 1, as not all spectroscopic data are publicly accessible. The spectra were collected from the following programs: the extended CDF-S faint X-ray source survey, GAMA, OzDES, VIPERS, Sloan Digital Sky Survey (SDSS), and DESI. Appendix A provides links for downloading these spectra. A brief description of each data set is given below.

The extended CDF-S faint X-ray source survey obtained spectroscopic redshifts of 283 Chandra sources up to $z \sim 4$. This program used the Very Large Telescope (VLT)/VIMOS and Keck/DEIMOS instruments. The VIMOS spectra cover a wavelength range of ∼5500–9600 Å with a spectral resolution of $R \sim 580$ (red grism) and ∼3700–6700 Å with $R \sim 180$ (blue grism), which is sufficient for measurements of the width of the broad lines. The DEIMOS spectra cover ∼4600–9700 Å and have a spectral resolution of $R \sim 2000$ (J. D. Silverman et al. 2010).

OzDES is a spectroscopic survey aiming to obtain the redshifts of DES sources using the 4 m Anglo-Australian Telescope with a Two-degree Field (2dF) multi-object fiber positioner. This instrument covers ∼3800–8900 Å with a spectral resolution of $R \sim 1800$ (M. J. Childress et al. 2017).

GAMA is a large spectroscopic survey of low-redshift galaxies. It covers galaxies of $z \lesssim 0.8$ with $r < 19.8$ mag. Its spectra cover a wavelength range of ∼3470–8850 Å. Its resolution ranges from $R \sim 1000$ at the blue end to $R \sim 1600$ at the red end, with a pixel size of 1.04 Å (J. Liske et al. 2015).

VIPERS is a public extragalactic redshift survey using the VLT/VIMOS instrument. This project obtained the photometry, spectra, and redshifts of galaxies bounded by $i_{AB} < 22.5$ with a redshift range $0.5 < z < 1.2$. Its spectra cover ∼5500–9500 Å with a resolution of $R \sim 220$ (M. Scodeggio et al. 2018).

SDSS is a wide-field spectroscopic survey, covering galaxies and quasars using various selection methods depending on the specific SDSS survey subset. Its spectroscopy spans approximately 3600–9800 Å, with a spectral resolution of $R \sim 2000$ (C. P. Ahn et al. 2012; A. Almeida et al. 2023).

DESI is another ongoing wide-field spectroscopic survey that targets galaxies, quasars, and Milky Way stars. The instrument provides spectral coverage from approximately 3600–9800 Å with a resolution of $R \sim$ 2000–5500 (DESI Collaboration et al. 2024).

4.2. Flux Calibration and Data Cleaning

In total, we have 1040 spectra with varying quality and wavelength coverage. Below, we outline our procedure for

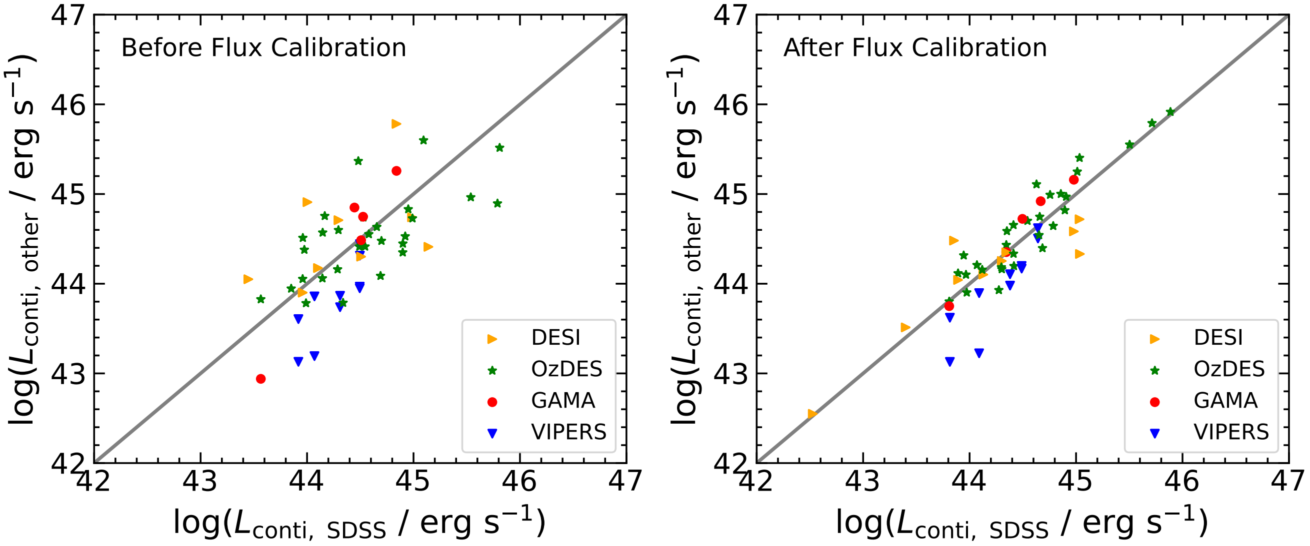

Figure 6. Demonstration of absolute flux calibration of our spectra. Each data point is a single DES-SN variable AGN with one spectrum from SDSS and at least one from another source. The bolometric luminosity from SDSS spectral continua is plotted against the bolometric luminosity from other spectra (see Table 1 for the data source list) before (left) and after (right) performing absolute flux calibration to the W. G. Hartley et al. (2022) photometry. Although AGN variability can contribute to some of the scatter across surveys, our resulting flux-calibrated spectra appear to be more consistent, as evidenced by the significantly reduced scatter. The right panel only includes those with successful flux calibration.

calibrating and cleaning the data. A reliable estimate of flux uncertainties is crucial for least squares minimization and χ^2 estimation (C. J. Burke et al. 2024b). When an error spectrum is not provided, we approximate uncertainties using the median absolute deviation of the flux spectrum. Wherever possible, we apply data quality masks to account for artifacts and spectral gaps. Each spectrum's fitting results are visually inspected. For sources with multiple spectra, if more than one provides a valid black hole mass estimate, we select the spectrum with the highest signal-to-noise ratio (S/N). We deliberately avoid stacking spectra from different surveys for two reasons: (1) combining spectra with different spectral resolutions introduces complications, and (2) lower signal-to-noise spectra often have poorer spectrophotometric calibration, which would propagate through the stack.

Accurate flux calibration is essential for deriving virial black hole masses, as these depend on continuum or broad-line luminosities. To minimize systematic differences between spectra from various surveys and instruments, we first apply absolute flux calibration to each spectrum. Specifically, we integrate each spectrum over the available DES+VIDEO *ugrizJHK*$_S$ bands to generate synthetic photometry, then scale it by the error-weighted mean ratio between synthetic and DES+VIDEO photometry. This method is widely used in the literature (e.g., R. P. Mallery et al. 2012). Figure 6 illustrates the improved consistency in spectral calibration across sources with multiple spectra from different surveys and instruments after applying absolute flux calibration with DES+VIDEO photometry.

Other data reduction challenges, such as residual instrumental sensitivity variations, are more difficult to correct. Additionally, we do not account for the effects of variability in the spectra. Based on the scatter observed in Figure 6, we estimate a 1σ uncertainty of approximately 10% in the final absolute flux calibration.

4.3. Spectral Modeling

We fit the continuum and emission lines in each 1D spectrum using a modified version of the publicly available PYQSOFIT code (H. Guo et al. 2018; Y. Shen et al. 2019), which has been widely used to analyze SDSS quasar properties (Y. Shen et al. 2011; Q. Wu & Y. Shen 2022). However, unlike the SDSS quasar sample, many of our spectra exhibit a significant host galaxy contribution. This is not unexpected, given that our sample consists of fainter quasars that are more host dominated, whereas the SDSS quasar sample is limited to $i < 20$. We caution that the host fraction in PYQSOFIT is limited by the wavelength range of spectra and template degeneracies and reddening. Consistently estimating the AGN and host contributions in spectroscopy and SED fitting is beyond the scope of this work.

We first perform quasar/host galaxy decomposition using principal component analysis (PCA) with host galaxy templates from G. Bruzual & S. Charlot (2003). After subtracting any significant host galaxy component, we model the quasar continuum as a blue power law combined with a third-order polynomial to account for reddening. If including Fe II emission templates (M. Vestergaard & B. J. Wilkes 2001) improves the reduced χ^2 of the continuum fit by at least 20%, they are incorporated into the model. The total model consists of the continuum and single or multiple Gaussian components for the emission lines.

Since uncertainties in the continuum model can affect measurements of weak emission lines, we first fit the global continuum in emission-line-free regions. We then fit multiple Gaussian components to the continuum-subtracted spectra in localized regions around the Hα, Hβ, Mg II, and C IV emission lines. Given the lower AGN luminosities and reduced continuum S/Ns, due to the higher redshifts and faintness of our sources, it is challenging to reliably separate the AGN continuum from the host galaxy contribution. Following C. J. Burke et al. (2024b), we use broad-line luminosities rather than AGN continuum luminosities to estimate black hole masses.

4.4. Deriving Black Hole Masses

Following Y. Shen et al. (2011), we estimate black hole masses using the single-epoch virial method (e.g., J. E. Greene

Table 2
Properties of DES-SN Variable AGNs from SED and Spectral Fitting Analysis

ID (1)	R.A. (2) (deg)	Decl. (3) (deg)	g-mag (4) (AB mag)	$z_{\rm best}$ (5)	$z_{\rm ph}$ (6)	$\log L$ (7) ($\log$ erg s^{-1})	$\log M_{\rm BH}$ (8) ($\log M_\odot$)	$\log M_{\rm BH,err}$ (9) ($\log M_\odot$)	$\log M_*$ (10) ($\log M_\odot$)	$\log M_{*,\rm err}$ (11) ($\log M_\odot$)	SF$_{\rm ex}$ (12)	χ^2_ν (13)	Class (14)
1	52.1408	−27.1823	23.7	1.02	1.02	⋯	⋯	⋯	10.96	0.06	1.4	4.8	⋯
2	52.4633	−27.1826	23.4	0.24	0.24	⋯	⋯	⋯	8.63	0.24	1.0	1.6	⋯
3	52.436	−27.1854	23.4	1.09	1.09	⋯	⋯	⋯	10.39	0.12	0.9	3.0	⋯
4	52.1894	−27.1881	21.5	1.3	1.3	⋯	⋯	⋯	10.16	0.59	1.3	6.3	⋯
⋮	⋯	⋯	⋯	⋯	⋯	⋯	⋯	⋯	⋯	⋯	⋯	⋯	⋯
706	36.3473	−5.0628	19.8	0.1909	0.2	⋯	⋯	⋯	10.47	0.11	9.6	6.6	⋯

Note. Column (1): Identifier from Table 4 of C. J. Burke et al. (2022). Column (2): R.A. Column (3): Decl. Column (4): g-band AB magnitude. Column (5): Best redshift. Column (6): Photometric redshift. Column (7): Bolometric luminosity from the spectral continuum. Column (8): Virial black hole mass. Column (9): Error of virial black hole mass. Column (10): Inferred CIGALE stellar mass. Column (11): Error of inferred CIGALE stellar mass. Column (12): Excess star formation over an AGN-dominated model (if >1.2, stellar masses are considered reliable). Column (13): Best-fit reduced CIGALE model χ^2 (recommend <5). Column (14): Visual classification of spectrum (see Section 4.5). All uncertainties are 1σ statistical errors from fitting. This table is published in its entirety in the published version. Only a portion is shown here.

(This table is available in its entirety in machine-readable form in the online article.)

& L. C. Ho 2005), which relies on broad emission lines. This method assumes that the broad-line region (BLR) is virialized, using the broad-line full width at half-maximum (FWHM) as a proxy for the virial velocity and the broad-line or continuum luminosity as an indicator of the BLR radius. Given the spectral quality of some of our sources (Appendix B), the continuum luminosities are not always well constrained. Therefore, we use broad-line luminosities instead of the continuum to estimate black hole masses. Under these assumptions, the black hole mass can be determined using the following equation:

$$\log\left(\frac{M_{\rm BH}}{M_\odot}\right) = a + b\log\left(\frac{L_{\rm br}}{10^{44}\ {\rm erg\ s^{-1}}}\right) + 2\log\left(\frac{{\rm FWHM}_{\rm br}}{\rm km\ s^{-1}}\right) \tag{1}$$

where $L_{\rm br}$ and FWHM$_{\rm br}$ are the broad-line luminosity and FWHM with an intrinsic scatter of $\sim$0.4 dex in black hole mass (e.g., M. Vestergaard & B. M. Peterson 2006). The coefficients a and b are empirically calibrated against local AGNs with black hole masses measured from reverberation mapping. We adopt the line calibrations from Y. Shen et al. (2011) derived by M. S. Shaw et al. (2012):

$$(a, b) = (1.63, 0.49), \quad {\rm H}\beta \tag{2}$$

$$(a, b) = (1.70, 0.63), \quad {\rm Mg\ II} \tag{3}$$

$$(a, b) = (1.52, 0.46), \quad {\rm C\ IV}. \tag{4}$$

For low-redshift sources, the broad Hα black hole masses are estimated as in Y. Shen et al. (2011) following J. E. Greene & L. C. Ho (2005):

$$\log\left(\frac{M_{\rm BH}}{M_\odot}\right) = 0.379 + 0.43\log\left(\frac{L_{\rm br}}{10^{42}\ {\rm erg\ s^{-1}}}\right) + 2.1\log\left(\frac{{\rm FWHM}_{\rm br}}{\rm km\ s^{-1}}\right). \tag{5}$$

Following Y. Shen et al. (2011), we determine a fiducial or preferred "best" black hole mass based on the ordering described above, considering factors such as wavelength coverage, redshift, and line S/N. We include black hole mass estimates only when the broad-line component is detected with S/N > 2, as defined in C. J. Burke et al. (2024a). If multiple spectra provide valid black hole mass estimates for the same source, we select the spectrum with the highest median per-pixel S/N.

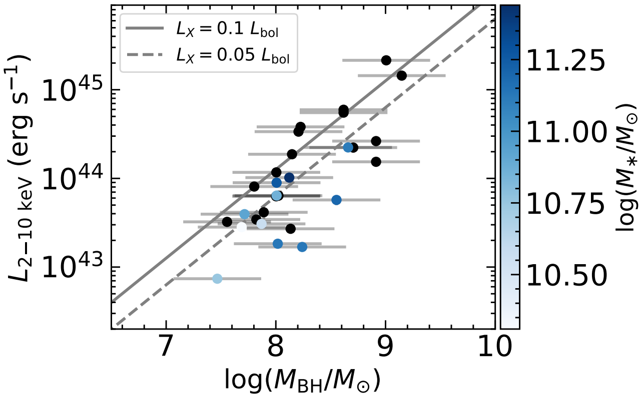

Figure 7. The 2−10 keV X-ray luminosities plotted against our measured broad-line black hole masses. The points are color coded by their stellar mass when it is considered reliable. Black points have unreliable stellar masses. An uncertainty of 0.4 dex is assumed for the black hole masses.

Although an extinction curve is fitted before measuring line luminosities, C IV and Mg II-based black hole masses are expected to be more affected by intrinsic reddening compared to Hβ-based masses (Y. Shen et al. 2019). The extinction is largely degenerate with the intrinsic spectral slope of the AGN continuum, and therefore difficult to quantify with PYQSOFIT. From our CIGALE best-fitted internal extinction values, we find $E(B-V) < 0.3$, which is generally consistent with Type 1 AGNs. Some of these systematic effects may be partially accounted for in the virial coefficients (Y. Shen & X. Liu 2012).

4.5. *Visual Spectral Classification*

Alongside our automated broad-line detection and fitting approach, we have visually inspected each spectrum to identify AGN signatures and provide initial classifications. Sources

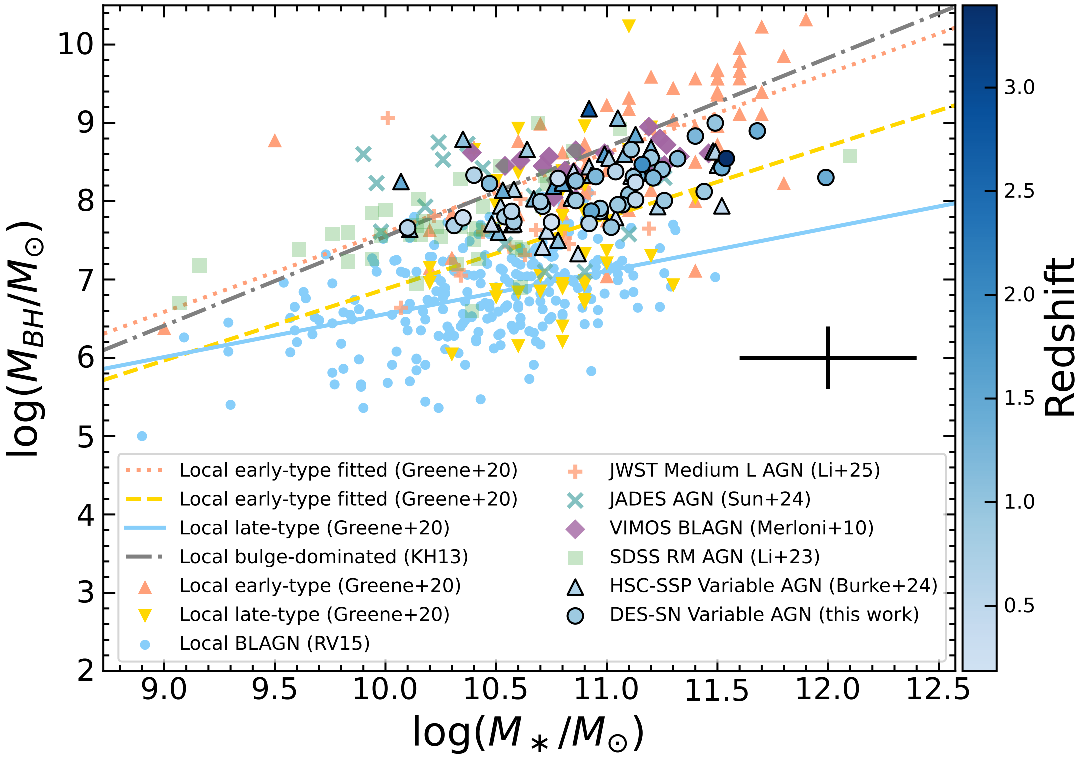

Figure 8. M_{BH}–M_* relation for the DES-SN (circle symbols) and HSC-SSP (triangle symbols) AGNs with reliable black hole mass estimates and reliable stellar masses from this work. Points are shaded by redshift. We assume uncertainties of ∼0.4 dex on the black hole masses. The typical uncertainties in our data are shown in the lower right corner. Data for AGN samples are overplotted with different symbols (A. Merloni et al. 2010; J. I. H. Li et al. 2023; C. J. Burke et al. 2024b; Y. Sun et al. 2024; J. Li et al. 2025). The local M_{BH}–M_* relation for inactive elliptical galaxies is plotted as a red dotted line and for inactive spiral galaxies as a dashed yellow line (J. E. Greene et al. 2020). The local M_{BH}–M_* relation for AGNs is plotted as a solid blue line (A. E. Reines & M. Volonteri 2015).

displaying at least one broad emission line are classified as "broad-line" objects. The remaining spectra, which lack clear AGN features, are either host dominated or have low signal to noise. Given the varying quality of spectrophotometric calibrations, we do not attempt to identify AGN continuum features.

In total, 174 sources exhibit AGN features, while 90 do not show obvious AGN-like characteristics, indicating either that they comprise host-dominated spectra or significant noise. These classifications are listed in Table 2. However, the absence of detected AGN spectral features does not necessarily mean an AGN is not present. For instance, the source could be in a host-dominated phase due to variability, or the observed spectrum may not cover any broad emission lines at the given redshift.

4.6. X-Ray Properties

To estimate the rough accretion rates of our sources, we utilize matched X-ray data from the Chandra Source Catalog and/or the XMM-Newton serendipitous survey catalog. The X-ray fluxes are converted to luminosities (uncorrected for absorption) using

$$L_{2-10\,\mathrm{keV}} = 4\pi d^2\,(1+z)^{\Gamma-2}\frac{10^{2-\Gamma} - 2^{2-\Gamma}}{E_2^{2-\Gamma} - E_1^{2-\Gamma}} f_{E_1-E_2}, \qquad (6)$$

where $f_{E_1-E_2}$ is the flux in keV given in the Chandra Source Catalog or XMM-Newton serendipitous survey catalog between energies E_1 and E_2 in keV. We take $\Gamma = 1.8$, which is typical for low-luminosity AGNs (e.g., L. C. Ho 2009). While a rough correction for absorption can be done using different energy bands and assuming a spectral shape for the AGN, we prefer to avoid these assumptions and leave detailed X-ray property investigations to future work.

Figure 7 presents the X-ray luminosities plotted against our broad-line black hole masses. The X-ray luminosities, which are typically $\gtrsim 10^{43}$ erg s^{-1}, exceed the levels expected from X-ray binary populations (B. D. Lehmer et al. 2019). Applying a standard bolometric correction of $L_{\mathrm{bol}}/L_{2-10\,\mathrm{keV}} = 10$ (F. Duras et al. 2020), we find that the sources have a typical (median) Eddington ratio of ∼0.05, which is slightly lower than the median ∼0.1 Eddington ratio reported by H. Suh et al. (2020). Our estimated Eddington ratios and black hole masses align well with expectations, given the known correlation between these parameters and optical variability amplitude (e.g., C. L. MacLeod et al. 2010). This is consistent with the typical variability amplitude of DES-SN AGNs, which is around 0.1 mag.

5. M_{BH}–M_* Relation

Figure 8 presents the M_{BH}–M_* relation, and Figure 9 shows M_{BH}–M_* versus redshift for our sample of DAVOS variability-selected AGNs with reliable stellar masses derived from SED fitting and virial black hole masses measured from our spectroscopic database. Figure 10 shows the distribution of black hole masses versus reshift, with Figure 11 showing example spectra from this work. The DES-SN variable AGN stellar masses and black hole masses come from this work, and the HSC-SSP variable AGN stellar masses and black hole masses are taken from C. J. Burke et al. (2024b). For our DAVOS AGNs in the combined DES-SN and HSC-SSP sample

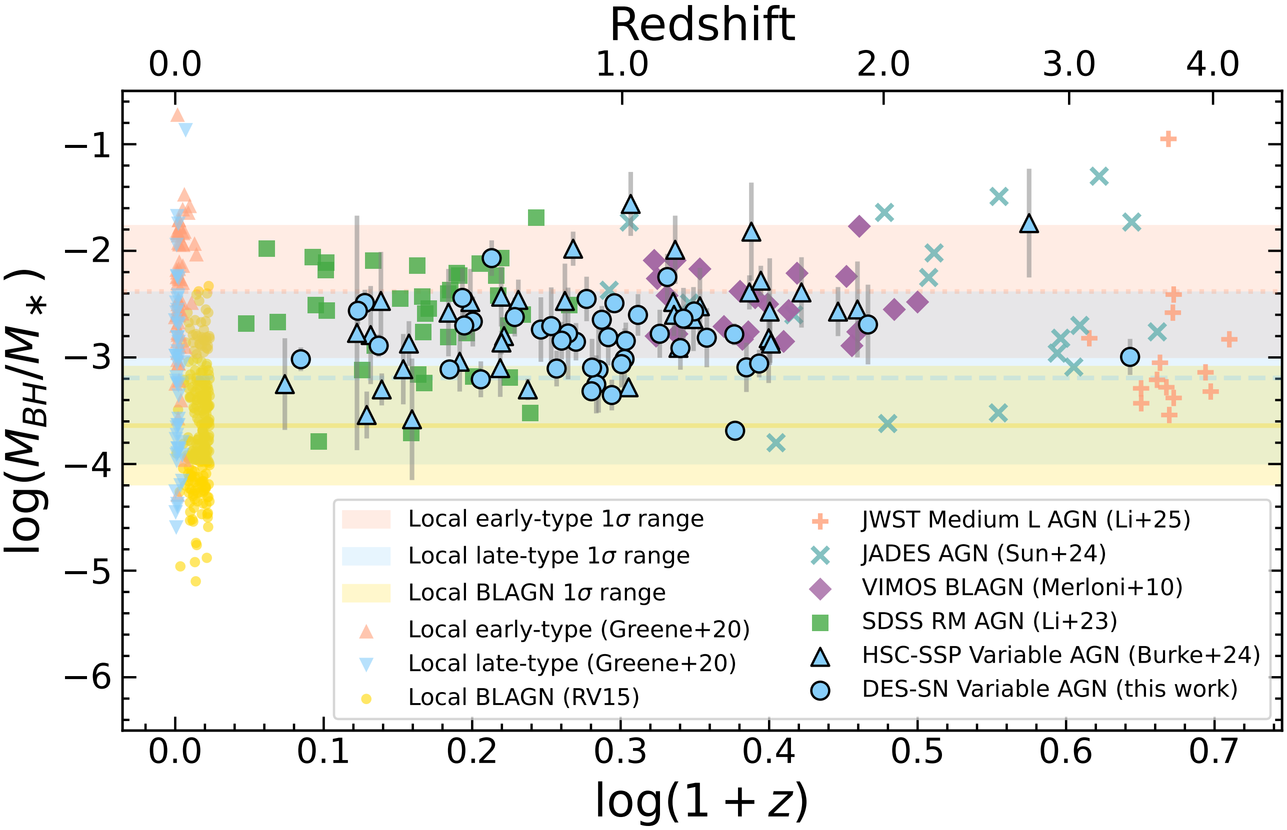

Figure 9. Summary of $M_{\rm BH}$–M_* vs. redshift up to $z \sim 4$. The DES-SN (circle symbols) and HSC-SSP (triangle symbols) AGNs with reliable black hole mass estimates and reliable stellar masses are plotted in blue symbols with black borders. We include J. Li et al. (2025), Y. Sun et al. (2024), A. Merloni et al. (2010), C. J. Burke et al. (2024b), J. I. H. Li et al. (2023) samples, along with local galaxies (J. E. Greene et al. 2020) and local AGNs (A. E. Reines & M. Volonteri 2015) for comparison. The 1σ range of the local early-type galaxies, late-type galaxies, and AGNs is plotted as red, yellow, and blue spans with dotted, dashed, and solid lines, respectively. Our AGN samples have a larger redshift span, making it easier to compare with different samples.

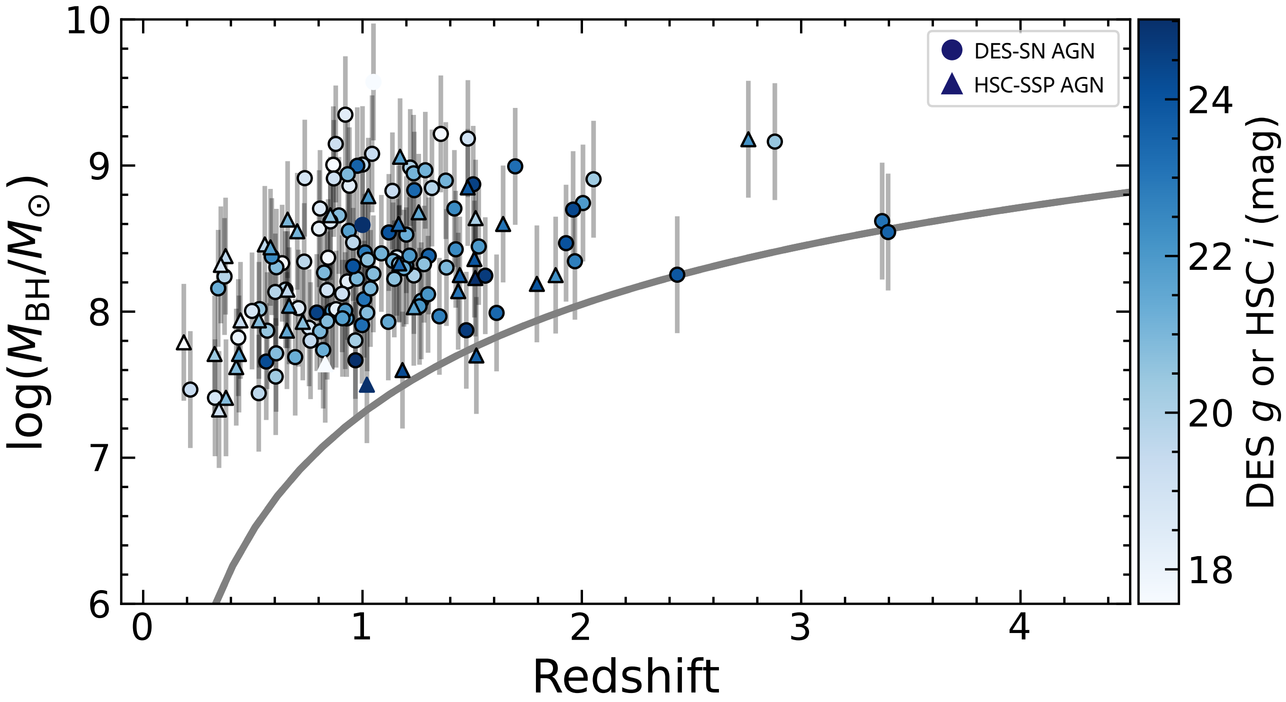

Figure 10. Black hole mass as a function of redshift for DES-SN (circle symbols) and HSC-SSP (triangle symbols) variable AGNs with reliable broad-line black hole mass estimates derived from broadband SED fitting using CIGALE. Each AGN is color shaded according to its DES g-band or HSC i-band apparent magnitude. The gray curve represents the theoretically predicted detection limit, which extends deeper than the black hole mass detection limit.

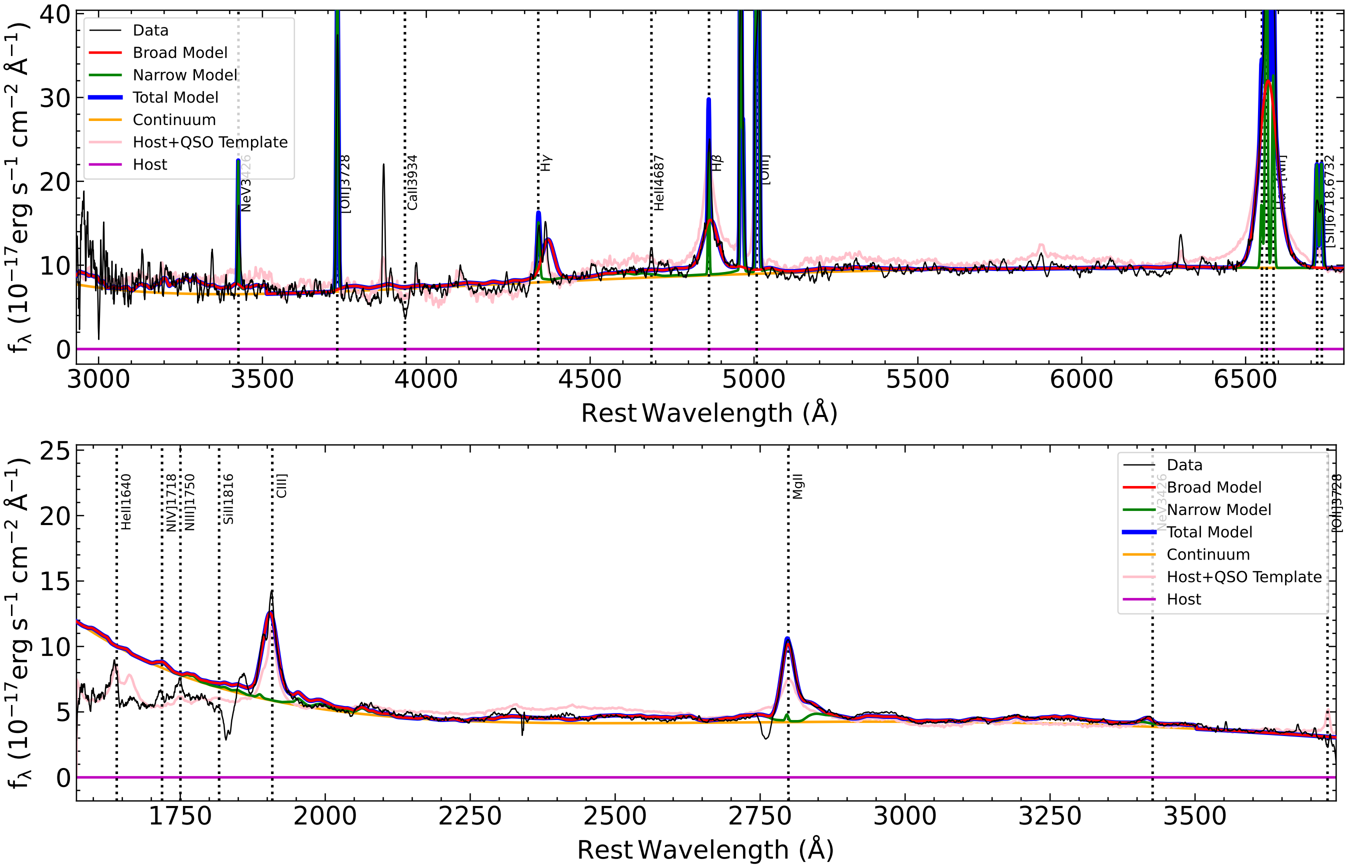

Figure 11. Spectral fitting results for C. J. Burke et al. (2022) ID 697 (upper panel) and ID 399 (bottom panel). The source in the upper panel is the lowest reliable stellar mass in our spectroscopic sample of $M_* \sim 10^{10} M_\odot$. The source in the lower panel is an example of a brighter AGN (showing blueshifted absorption features) with an unreliable stellar mass. The spectral data (black) is plotted with the model fitting components: polynomial+power-law continuum (orange), total line model flux (blue), broad-line model flux (red), narrow-line model flux (green) fitted host+QSO template (pink), and fitted host template (magenta). In both cases, the PCA-derived host fluxes are small. The resulting broad-line black hole mass for the source in the lower panel is $M_{\rm BH} \sim 10^{8.3} M_\odot$ at $z = 1.383$. The black hole mass for the source in the upper panel is $M_{\rm BH} \sim 10^{7.5} M_\odot$ at $z = 0.215$.

with reliable black hole and stellar masses at $z \sim 0.1$–3.4 (median redshift ∼0.8), the relation aligns more closely with that of local inactive elliptical galaxies (J. E. Greene et al. 2020) rather than local ($z < 0.055$) AGNs (A. E. Reines & M. Volonteri 2015). However, at lower redshifts, variability-selected AGNs appear to trend toward the local AGN relation, as seen in Figure 9. This trend, previously observed in HSC-SSP AGNs, is now confirmed with a larger sample size (C. J. Burke et al. 2024b).

There is a notable absence of sources with very massive black holes ($M_{\rm BH} \gtrsim 10^9 M_\odot$) in our sample, compared to the local inactive elliptical galaxy population. We attribute this to the difficulty in obtaining reliable stellar masses for highly luminous AGNs with high AGN fractions, where host galaxy light is overwhelmed by the AGN emission.

6. Discussion

6.1. Impact of Selection Biases

At first glance, this result may suggest an evolution in the $M_{\rm BH}$–M_* relation for AGNs with redshift. Such an evolution could be linked to changes in host SFRs or black hole accretion activity, as both peak at $z \sim 2$ (M.-Y. Zhuang & L. C. Ho 2023). However, A. Bongiorno et al. (2012) analyzed AGN activity and host SFRs in an X-ray and optically selected AGN sample up to $z \sim 3$ in the COSMOS field, finding no strong evidence for a direct connection between AGN activity and host star formation.

R. C. Hickox et al. (2014) suggest that the weak observed correlations between AGN luminosity and host galaxy properties can be understood as a timescale mismatch: AGN activity lasts for ∼Myr timescales, but star formation and stellar mass growth are averaged over ∼100 Myr timescales. Therefore, the lack of correlations in observations involving instantaneous AGN activity reflects the fact that AGN short-term variability washes out the underlying average trends. Using the EAGLE simulation, S. McAlpine et al. (2017) show that the time-averaged growth of black holes and galaxies follows a tight relation, even though instantaneous BHAR and SFR are mostly uncorrelated. Furthermore, weak trends seen in other studies (e.g., D. Lutz et al. 2010; D. G. Bonfield et al. 2011) could be attributed to the large scatter in the stellar mass and SFR estimates.

Measurements of the $M_{\rm BH}$–M_* relation are significantly affected by selection biases at both low and high redshifts (T. R. Lauer et al. 2007; Y. Shen & B. C. Kelly 2010; F. Shankar et al. 2019), as discussed in C. J. Burke et al. (2024b). Our spectroscopic sample includes spectra from various spectroscopic programs, each with different targeting criteria and spectral sensitivities. Additionally, we cannot reliably estimate stellar masses for optically luminous AGNs, making it challenging to quantify the impact of selection biases on our results.

Selection biases have been shown to introduce a false evolution in the $M_{\rm BH}$–M_* relation (T. R. Lauer et al. 2007; Y. Shen & B. C. Kelly 2010). Since our sample is selected based on AGN activity, it is inherently biased toward more luminous AGNs and larger black hole masses at higher redshifts. However, previous studies have found a similar $M_{\rm BH}$–M_* relation for X-ray and spectroscopically selected AGNs at comparable redshifts and higher AGN luminosities (A. Merloni et al. 2010; M.-Y. Zhuang et al. 2024). This suggests that the variable AGN population is unlikely to be probing a substantially different parameter space from the broader Type 1 AGN population.

Quantifying the effects of selection biases on our sample would require modeling the detectable AGN population at these redshifts (e.g., F. Pacucci et al. 2023; J. Li et al. 2025), but such an analysis depends on the true intrinsic scatter of the $M_{\rm BH}$–M_* relation, which remains uncertain. Possible origins of the scatter in the $M_{\rm BH}$–M_* relation include AGN variability, galaxy mergers, or SED-fitting uncertainties. The findings in this paper, we acknowledge, should be considered within the context of these limitations. Detailed modeling of selection biases is beyond the scope of this work.

6.2. Evolution in the M_{BH}–M_* *Relation?*

As noted by C. J. Burke et al. (2024b), the recently proposed model of F. Pacucci & A. Loeb (2024) predicts that black holes at $z \sim 0.5$–3 should be 3–10 times more massive than expected from the local AGN relation, which is broadly consistent with our findings. For example, the earlier models of black hole-galaxy coevolution, such as those by J. S. B. Wyithe & A. Loeb (2003) and N. Caplar et al. (2018), also predict a redshift evolution of the $M_{\rm BH}$–M_* relation that is attributed to self-regulated feedback, which limits black hole growth before quenching occurs at a critical $M_{\rm BH}/M_*$ threshold. Additionally, S. Dattathri et al. (2025) propose that the evolution of the mean relation is driven by the ratio of the black hole accretion rate to the SFR, $\dot{M}_{\rm acc}/\dot{M}_*$.

If our results are not significantly affected by selection effects, they indicate a possible redshift evolution in the $M_{\rm BH}$–M_* relation when compared to local AGNs (A. E. Reines & M. Volonteri 2015). However, our results are generally consistent with no evolution beyond $z \sim .05$ (Figure 9). However, the lack of any observed evolution beyond the local sample of A. E. Reines & M. Volonteri (2015) –despite the significant redshift evolution in the cosmic SFR density—seems to contradict these models. Perhaps differences in the sample selection of the A. E. Reines & M. Volonteri (2015) make these AGNs special in some way.

As pointed out by J. Li et al. (2025), the A. E. Reines & M. Volonteri (2015) local AGN sample is also subject to selection effects that could bias the inferred $M_{\rm BH}$–$M_\star$ relation. In particular, AGN-based samples may systematically miss the most massive black holes, which are preferentially hosted by quiescent, bulge-dominated galaxies (e.g., J. Kormendy & L. C. Ho 2013) that rarely appear in emission-line AGN surveys. This introduces a mass-dependent selection, where relatively low-mass black holes in star-forming host galaxies are well represented, but the upper end of the black hole mass distribution is underrepresented. The resulting relation can therefore appear offset to lower black hole masses at fixed stellar mass, relative to relations calibrated on quiescent galaxies with dynamical black hole mass measurements. This bias provides a natural explanation for the discrepancy highlighted in Figure 9, where the local AGN fall systematically below other data. Furthermore, it is possible that systematic errors in the black hole or stellar masses or model photometry are partly responsible for these discrepancies.

7. Conclusions

Using the sample of variable AGNs selected from the DES-SN Deep Fields (C. J. Burke et al. 2022), we obtained improved multiwavelength photometry from DES+VIDEO (W. G. Hartley et al. 2022), GALEX, Wide-field Infrared Survey Explorer (WISE), and X-ray, and used an improved SED-fitting approach to estimate their stellar masses. We determined the reliability of the stellar mass estimates using the stellar emission strength at 1.2 μm, where the AGN emission is expected to be at a minimum (A. Merloni et al. 2010; C. J. Burke et al. 2024b). After constructing a database of publicly available spectra from the literature, we measured their virial black hole masses from the detected broad emission lines when the S/N is permitted. We place our variable AGNs on the $M_{\rm BH}$–M_* relation at $z \sim 0.1$–3.4 (median redshift of ∼0.8). The elevated $M_{\rm BH}/M_*$ ratios observed in variability-selected AGNs support scenarios where these SMBHs experienced early rapid growth compared to the A. E. Reines & M. Volonteri (2015) local AGNs. These results, combined with the high occupation fraction in local dwarf galaxies (C. J. Burke et al. 2025), are possibly consistent with a mixture of heavy seed formation channels.

This is a marked improvement over previous work (C. J. Burke et al. 2022) because we have obtained homogenized broad-line black hole mass estimates and improved the stellar mass estimates in this work. This allowed us to robustly place the sources on the $M_{\rm BH}$–M_* relation. Compared to previous work in the COSMOS field (C. J. Burke et al. 2024b), this study fills the gap at $z \lesssim 1.5$, forming a sample of variability-selected AGNs with well-sampled SEDs and black hole masses at $0.05 \lesssim z \lesssim 3$. Our results concur with previous findings using other AGN samples of more massive black holes at a given stellar mass than the local AGN relation would suggest. These confirm our previous conclusion that AGNs selected from optical variability are not vastly different from samples of AGNs selected from broad lines at similar redshifts at fixed luminosity (C. J. Burke et al. 2024b).

Using these results to assess the feasibility of such studies with the capabilities of the LSST Rubin Observatory, we demonstrate that black holes with $M_{\rm BH} \sim 10^8 M_\odot$ are detectable out to at least $z \sim 4$ in $M_* \sim 10^{11} M_\odot$ host galaxies using optical variability. Future work combining Rubin-selected AGNs and Euclid or Roman Space Telescope host galaxy imaging will increase the sample size of sources with reliable estimates of stellar masses from AGN+host decomposition, as joint analysis of high-resolution and time-resolved imaging can yield improved SED extraction of AGN host galaxies (P. Melchior et al. 2018; C. Ward et al. 2025).

We have not investigated narrow emission-line ratio diagnostics in this paper. Given the varying wavelength coverage and redshifts of the spectra, the majority of the spectra do not cover both the Hβ and Hα spectral complexes. The majority of the sources have AGN features in their spectra (either a broad-line detection or Ne V emission line), but a significant fraction are either too noisy or host-dominated to detect any obvious AGN features. Some of the latter could be false positives (i.e., non-AGN galaxy or transient interlopers). This work highlights the challenges of obtaining sufficient spectroscopy to investigate low-luminosity AGNs at the redshifts that LSST Rubin will unveil.

The large scatter in the M_{BH}–M_* relation likely reflects the diversity of growth channels of AGN host galaxies and/or the mismatch between growth timescales of the black hole and star formation (e.g., R. C. Hickox et al. 2014). This and the relatively low redshift of the sample, significantly later than the principal seeding epoch, expected to be at $z > 10$, make it difficult to place direct meaningful constraints on SMBH seeding pathways. However, estimates of the occupation fraction in low-mass galaxies have been shown to be a reliable proxy of high-redshift seeding from previous modeling work (M. Volonteri & P. Natarajan 2009; A. Ricarte & P. Natarajan 2018). Observational studies such as this one and future work spanning an even wider range of redshifts, host galaxy masses, and with diverse selection techniques are nevertheless important to anchor these models of SMBH seeding and feedback over cosmic time (e.g., M. Volonteri & P. Natarajan 2009; A. Ricarte & P. Natarajan 2018).

Acknowledgments

We thank the anonymous referee for a careful review and for providing comments that improved this work. This research has made use of the SIMBAD database (M. Wenger et al. 2000), operated at CDS, Strasbourg, France. This research made use of ASTROQUERY (A. Ginsburg et al. 2019), SIMBAD (M. Wenger et al. 2000), and VizieR (F. Ochsenbein et al. 2000).

C.J.B. is supported by a National Science Foundation (NSF) Astronomy and Astrophysics Postdoctoral Fellowship under award No. AST-2303803. This material is based upon work supported by the NSF under award No. 2303803. This research award to NSF is partially funded by a generous gift of Charles Simonyi to the NSF Division of Astronomical Sciences. The award is made in recognition of significant contributions to the Rubin Observatory's LSST. Y.L. and X.L. acknowledge support from the University of Illinois Campus Research Board award No. RB22065 and NSF grant No. AST-2308077. P.N. acknowledges support from the Gordon and Betty Moore Foundation and the John Templeton Foundation that fund the Black Hole Initiative (BHI) at Harvard University, where she serves as one of the PIs.

This work makes use of data from the Chandra X-ray Observatory, specifically CDF-S.

This work is based in part on observations made with the Spitzer Space Telescope, operated by the Jet Propulsion Laboratory, California Institute of Technology, under contract with NASA.

We use data from the VIMOS VLT Deep Survey (VVDS), which provides magnitude-limited spectroscopic redshifts over wide, deep, and ultra-deep fields.

This paper uses data from the VIMOS Public Extragalactic Redshift Survey (VIPERS). VIPERS has been performed using the ESO Very Large Telescope, under the "Large Programme" 182.A-0886. The participating institutions and funding agencies are listed at http://vipers.inaf.it.

GAMA is a joint European-Australasian project based around a spectroscopic campaign using the Anglo-Australian Telescope. The GAMA input catalog is based on data from the SDSS and the UKIRT Infrared Deep Sky Survey. Complementary imaging was obtained by GALEX MIS, VST KiDS, VISTA VIKING, WISE, Herschel-ATLAS, GMRT, and ASKAP. GAMA is funded by the STFC (UK), the ARC (Australia), the AAO, and the participating institutions.

Funding for SDSS-V has been provided by the Alfred P. Sloan Foundation, the Heising–Simons Foundation, the National Science Foundation, and the Participating Institutions. SDSS acknowledges support and resources from the Center for High-Performance Computing at the University of Utah.

This research used data obtained with DESI. DESI construction and operations are managed by the Lawrence Berkeley National Laboratory. This material is based upon work supported by the US Department of Energy, Office of Science, Office of High-Energy Physics, under contract No. DE-AC02-05CH11231, and by the National Energy Research Scientific Computing Center, a DOE Office of Science User Facility under the same contract. Additional support for DESI was provided by the US NSF, Division of Astronomical Sciences, under contract No. AST-0950945 to the NSF's National Optical-Infrared Astronomy Research Laboratory; the Science and Technology Facilities Council of the United Kingdom; the Gordon and Betty Moore Foundation; the Heising–Simons Foundation; the French Alternative Energies and Atomic Energy Commission (CEA); the National Council of Humanities, Science and Technology of Mexico (CONAHCYT); the Ministry of Science and Innovation of Spain (MICINN); and by the DESI Member Institutions. The DESI collaboration is honored to be permitted to conduct scientific research on I'oligam Du'ag (Kitt Peak), a mountain with particular significance to the Tohono O'odham Nation. Any opinions, findings, and conclusions or recommendations expressed in this material are those of the author(s) and do not necessarily reflect the views of the US NSF, the US Department of Energy, or any of the listed funding agencies.

Appendix A
Data Availability

The publicly available spectra were collected from the following web pages:

1. CDF-S faint X-ray: https://member.ipmu.jp/john.silverman/CDFS_data.html and https://www.eso.org/~vmainier/cdfs_pub/
2. Spitzer/IRS ATLAS: https://www.denebola.org/atlas/
3. VVDS: http://cesam.lam.fr/vvds
4. VIPERS: http://vipers.inaf.it/
5. GAMA: https://www.gama-survey.org
6. OzDES: https://docs.datacentral.org.au/ozdes/overview/ozdes-data-release/
7. SDSS: https://dr18.sdss.org/optical/plate/search
8. DESI: https://datalab.noirlab.edu/desi/access.php

This paper employs a list of Chandra data sets, obtained by the Chandra X-ray Observatory, contained in DOI:10.25574/cdc.451.

This paper employs the SEIP Source List, obtained by the Spitzer Space Telescope and WISE (P. Capak 2019).

Appendix B
Reliability of Spectral Continuum Measurements

Spectra of AGNs with low bolometric luminosities of $L_{\rm bol} \lesssim 10^{45}$ erg s^{-1} have a significant contribution from the underlying host galaxy (Y. Shen et al. 2011; Y. Kimura et al. 2020). Reliably constraining the continuum luminosity from the AGN is an essential step for obtaining a virial black hole mass estimate. This is because the virial prescriptions use the AGN continuum luminosity as a proxy for the BLR luminosity (Y. Shen et al. 2011). PCA decomposition can constrain the quasar continuum for sources below $L_{\rm bol} \sim 10^{45}$ erg s^{-1} if the spectra are of sufficient quality (W. Ren et al. 2024). However, the quality of the spectra in our sample (calibration and S/N) varies considerably depending on the instrument and the spectral reduction/calibration. Following our previous work (C. J. Burke et al. 2024b), we test whether the quasar continuum luminosities are well constrained by computed virial black hole masses using both the broad-line luminosity (Equation (1)) or continuum luminosity approaches using the equation

$$\log\left(\frac{M_{\rm BH}}{M_\odot}\right) = a + b\log\left(\frac{\lambda L_\lambda}{10^{44}\ {\rm erg\ s^{-1}}}\right) + 2\log\left(\frac{{\rm FWHM_{br}}}{{\rm km\ s^{-1}}}\right), \tag{B1}$$

where λL_λ and FWHM$_{\rm br}$ are the continuum luminosity and broad-line FWHM. We adopt the continuum calibrations used in Y. Shen et al. (2011):

$$(a, b) = (0.910, 0.50), \quad {\rm H}\beta, \tag{B2}$$

$$(a, b) = (0.740, 0.62), \quad {\rm Mg\ II}, \tag{B3}$$

$$(a, b) = (0.660, 0.53), \quad {\rm C\ IV}. \tag{B4}$$

These single-epoch relations have an intrinsic scatter of ∼0.4 dex in black hole mass. If the AGN continuum luminosities are well constrained, we expect the two approaches to yield consistent results within systematic uncertainties between the two prescriptions. For our sample, we found that two prescriptions typically yield similar results. However, the continuum-based black hole masses are often underestimated at the low-mass end when the AGN continuum is not well constrained, as shown in Figure 12. Therefore, as in C. J. Burke et al. (2024b), we adopt black hole masses estimated from the broad-line luminosity throughout this work from Equation (1).

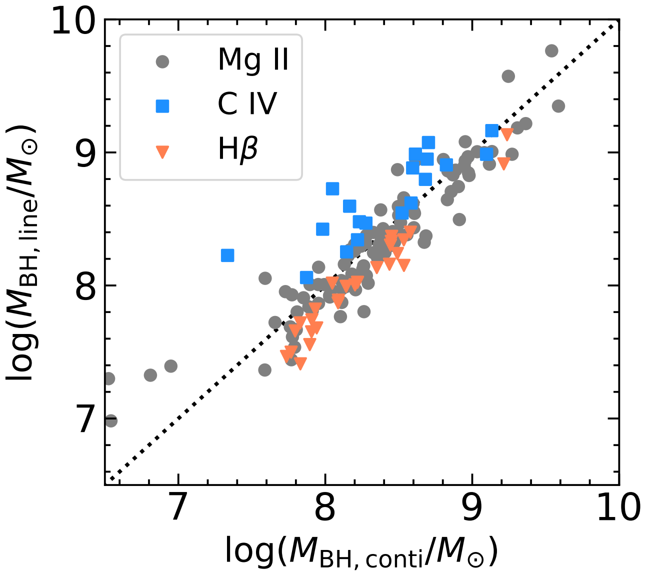

Figure 12. Black hole masses estimated from the broad-line luminosity vs. (y-axis) AGN continuum luminosity (x-axis). The black hole masses from the AGN continuum luminosity are susceptible to a few catastrophically underestimated masses when the AGN continuum is not well constrained.

Appendix C
Improvement of Stellar Mass Estimates

We deem our stellar masses reliable if the stellar emission dominates over the AGN emission at 1.2 μm, using the criteria SF$_{\rm ex} > 1.2$ (C. J. Burke et al. 2024b). In cases where the AGN emission dominates, the SED-fitting-derived stellar masses are likely to have a large variance. To investigate this improvement, we plot the stellar mass calculated from this work and the stellar masses from C. J. Burke et al. (2022) in Figure 13, where we use the SF$_{\rm ex} > 1.2$ criteria to ensure that our stellar masses are reliable. The figure indicates that C. J. Burke et al. (2022) generally underestimated the stellar masses, sometimes by up to 4 orders of magnitude. However, most of the blue points (stellar masses considered reliable by C. J. Burke et al. 2022) lie on the $y = x$ line. It is reassuring that the C. J. Burke et al. (2022) reliable stellar masses are generally consistent with ours. However, we conclude that more of our stellar masses are reliable. We attribute this primarily to the increased wavelength coverage (i.e., the inclusion of X-ray, ultraviolet, and infrared photometry) in our work.

We also show the distribution of bolometric luminosity and black hole mass versus SF$_{\rm ex}$ in Figure 14, which confirms that sources with unreliable stellar masses (dominated by AGN emission) tend to be higher mass/luminosity. In particular, all

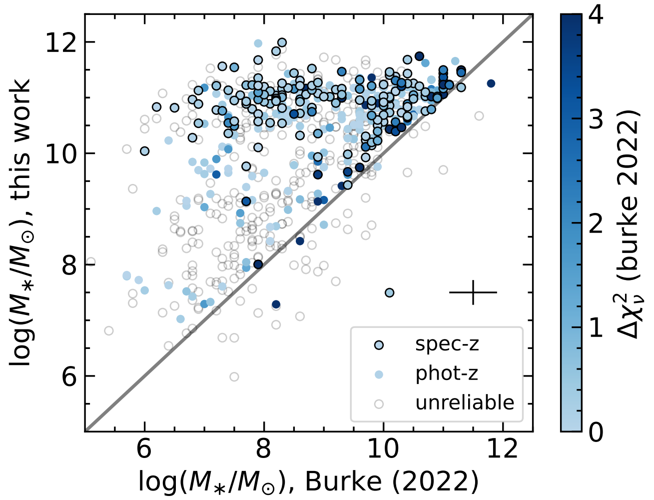

Figure 13. Stellar masses estimated using our improved approach (this work) vs. the stellar masses calculated by C. J. Burke et al. (2022). The gray circles are unreliable stellar masses ($\chi^2 > 5$ or star formation excess >1.2 (same as Figure 10). The circles with solid borders are sources with reliable stellar masses with spectroscopic redshifts. The circles without borders are reliable stellar masses with photometric redshifts. The circles are colored by the improvement in fit quality measure $\Delta\chi^2_\nu$ as calculated by C. J. Burke et al. (2022). The bluer colors are more reliable stellar masses, as determined by C. J. Burke et al. (2022). A typical error bar is shown on the right. More of our stellar masses are reliable using the improved approach. A $y = x$ line is plotted in gray.

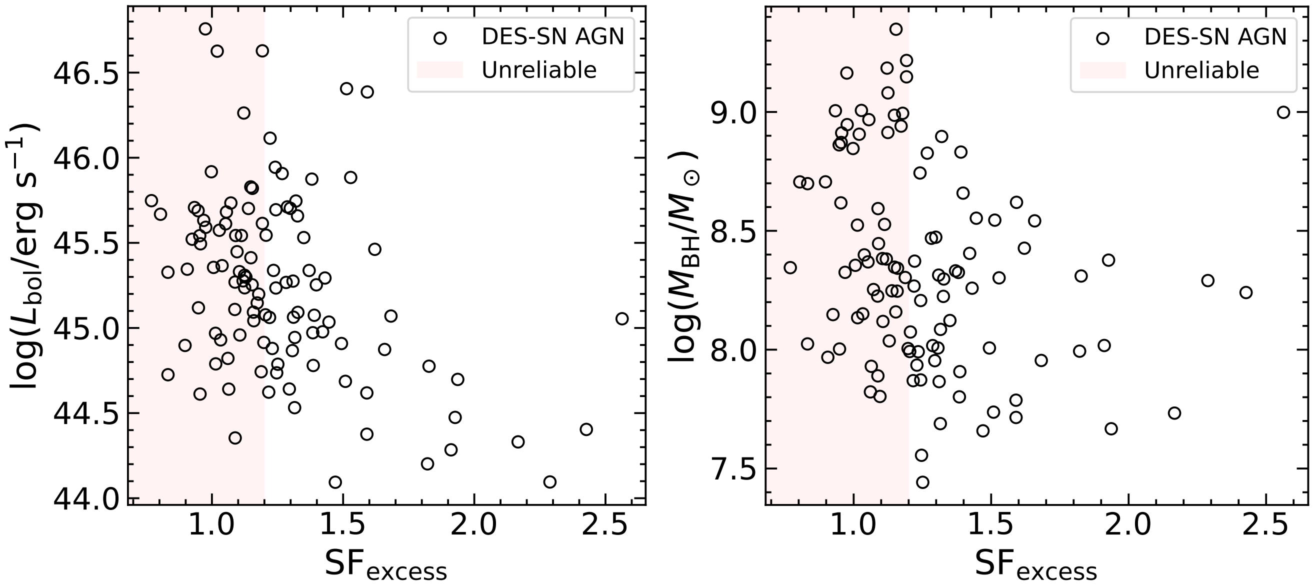

Figure 14. Distribution of star formation excess. The region marked as light red (star formation excess <1.2) is considered unreliable because these AGNs are dominated by AGN emission. Left panel: star formation excess vs bolometric luminosity; Right panel: star formation excess vs. black hole mass.

AGNs with $M_{\rm BH} \gtrsim 10^9 M_\odot$ do not have reliably measured stellar masses. This results in an additional mild selection bias in our final sample.

ORCID iDs

Yichen Liu https://orcid.org/0000-0003-4247-0169
Colin J. Burke https://orcid.org/0000-0001-9947-6911
Diego Miura https://orcid.org/0009-0009-9486-3053
Xin Liu https://orcid.org/0000-0003-0049-5210
Qian Yang https://orcid.org/0000-0002-6893-3742
Priyamvada Natarajan https://orcid.org/0000-0002-5554-8896
Charlotte A. Ward https://orcid.org/0000-0002-4557-6682

References

Ahn, C. P., Alexandroff, R., Allende Prieto, C., et al. 2012, ApJS, 203, 21
Ahumada, R., Allende Prieto, C., Almeida, A., et al. 2020, ApJS, 249, 3
Alam, S., Albareti, F. D., Allende Prieto, C., et al. 2015, ApJS, 219, 12
Almeida, A., Anderson, S. F., Argudo-Fernández, M., et al. 2023, ApJS, 267, 44
Baldassare, V. F., Geha, M., & Greene, J. 2018, ApJ, 868, 152
Baldassare, V. F., Geha, M., & Greene, J. 2020, ApJ, 896, 10
Baldry, I. K., Liske, J., Brown, M. J. I., et al. 2018, MNRAS, 474, 3875
Bianchi, L., Shiao, B., & Thilker, D. 2017, ApJS, 230, 24
Bogdán, Á., Goulding, A. D., Natarajan, P., et al. 2023, NatAs, 8, 126
Bonfield, D. G., Jarvis, M. J., Hardcastle, M. J., et al. 2011, MNRAS, 416, 13
Bongiorno, A., Merloni, A., Brusa, M., et al. 2012, MNRAS, 427, 3103
Boquien, M., Burgarella, D., Roehlly, Y., et al. 2019, A&A, 622, A103
Bruzual, G., & Charlot, S. 2003, MNRAS, 344, 1000
Burgarella, D., Buat, V., & Iglesias-Páramo, J. 2005, MNRAS, 360, 1413
Burke, C. J., Liu, X., & Shen, Y. 2024a, MNRAS, 527, 5356
Burke, C. J., Liu, X., Shen, Y., et al. 2022, MNRAS, 516, 2736
Burke, C. J., Liu, Y., Ward, C. A., et al. 2024b, ApJ, 971, 140
Burke, C. J., Natarajan, P., Baldassare, V. F., & Geha, M. 2025, ApJ, 978, 77
Burke, C. J., Shen, Y., Chen, Y.-C., et al. 2020, ApJ, 899, 136
Burke, C. J., Shen, Y., Liu, X., et al. 2023, MNRAS, 518, 1880
Calzetti, D., Armus, L., Bohlin, R. C., et al. 2000, ApJ, 533, 682
Capak, P. 2019, Spitzer Enhanced Imaging Products (SEIP) Source List,
Caplar, N., Lilly, S. J., & Trakhtenbrot, B. 2018, ApJ, 867, 148
Chabrier, G. 2003, ApJL, 586, L133
Cheng, C., Huang, J.-S., Willmer, C. N. A., et al. 2021, ApJS, 256, 4
Childress, M. J., Lidman, C., Davis, T. M., et al. 2017, MNRAS, 472, 273
Ciesla, L., Charmandaris, V., Georgakakis, A., et al. 2015, A&A, 576, A10
Civano, F., Marchesi, S., Comastri, A., et al. 2016, ApJ, 819, 62
Conroy, C. 2013, ARA&A, 51, 393
Cooper, M. C., Yan, R., Dickinson, M., et al. 2012, MNRAS, 425, 2116
Dark Energy Survey Collaboration, Abbott, T., Abdalla, F. B., et al. 2016, MNRAS, 460, 1270
Dattathri, S., Natarajan, P., Porras-Valverde, A. J., et al. 2025, ApJ, 984, 122
DESI Collaboration, Adame, A. G., Aguilar, J., et al. 2024, AJ, 168, 58
Ding, X., Silverman, J., Treu, T., et al. 2020, ApJ, 888, 37
Draine, B. T., Aniano, G., Krause, O., et al. 2014, ApJ, 780, 172
Draine, B. T., & Li, A. 2007, ApJ, 657, 810
Duras, F., Bongiorno, A., Ricci, F., et al. 2020, A&A, 636, A73
Eales, S., Chapin, E. L., Devlin, M. J., et al. 2009, ApJ, 707, 1779
Evans, I. N., Primini, F. A., Glotfelty, K. J., et al. 2010, ApJS, 189, 37
Fabian, A. C. 2012, ARA&A, 50, 455
Garcet, O., Gandhi, P., Gosset, E., et al. 2007, A&A, 474, 473
Garilli, B., Guzzo, L., Scodeggio, M., et al. 2014, A&A, 562, A23
Ginsburg, A., Sipőcz, B. M., Brasseur, C. E., et al. 2019, AJ, 157, 98
Goulding, A. D., Greene, J. E., Setton, D. J., et al. 2023, ApJL, 955, L24
Greene, J. E., & Ho, L. C. 2005, ApJ, 630, 122
Greene, J. E., Strader, J., & Ho, L. C. 2020, ARA&A, 58, 257
Guo, H., Burke, C. J., Liu, X., et al. 2020, MNRAS, 496, 3636
Guo, H., Shen, Y., & Wang, S. 2018, PyQSOFit: Python Code to fit the Spectrum of Quasars, Astrophysics Source Code Library, ascl:1809.008
Haehnelt, M. G., Natarajan, P., & Rees, M. J. 1998, MNRAS, 300, 817
Halevi, G., Goulding, A., Greene, J., et al. 2019, ApJL, 885, L3
Harikane, Y., Zhang, Y., Nakajima, K., et al. 2023, ApJ, 959, 39
Hartley, W. G., Choi, A., Amon, A., et al. 2022, MNRAS, 509, 3547
Hernán-Caballero, A., & Hatziminaoglou, E. 2011, MNRAS, 414, 500
Hickox, R. C., Mullaney, J. R., Alexander, D. M., et al. 2014, ApJ, 782, 9
Ho, L. C. 2009, ApJ, 699, 626
Inoue, A. K. 2011, MNRAS, 415, 2920
Ivezić, Ž., Kahn, S. M., Tyson, J. A., et al. 2019, ApJ, 873, 111
Izumi, T., Matsuoka, Y., Fujimoto, S., et al. 2021, ApJ, 914, 36
Izumi, T., Onoue, M., Matsuoka, Y., et al. 2019, PASJ, 71, 111
Jarvis, M. J., Bonfield, D. G., Bruce, V. A., et al. 2013, MNRAS, 428, 1281
Just, D. W., Brandt, W. N., Shemmer, O., et al. 2007, ApJ, 665, 1004
Kessler, R., Marriner, J., Childress, M., et al. 2015, AJ, 150, 172
Kimura, Y., Yamada, T., Kokubo, M., et al. 2020, ApJ, 894, 24
Kocevski, D. D., Onoue, M., Inayoshi, K., et al. 2023, ApJL, 954, L4
Kokorev, V., Fujimoto, S., Labbe, I., et al. 2023, ApJL, 957, L7
Kormendy, J., & Ho, L. C. 2013, ARA&A, 51, 511
Kovács, O. E., Bogdán, Á., Natarajan, P., et al. 2024, ApJL, 965, L21
Lacy, M., Ridgway, S. E., Gates, E. L., et al. 2013, ApJS, 208, 24
Lauer, T. R., Tremaine, S., Richstone, D., & Faber, S. M. 2007, ApJ, 670, 249
Le Fèvre, O., Cassata, P., Cucciati, O., et al. 2013, A&A, 559, A14
Lee, J., Acevedo, M., Sako, M., et al. 2023, AJ, 165, 222
Lehmer, B. D., Eufrasio, R. T., Tzanavaris, P., et al. 2019, ApJS, 243, 3

Leitherer, C., Li, I. H., Calzetti, D., & Heckman, T. M. 2002, ApJS, 140, 303
Li, J., Shen, Y., & Zhuang, M.-Y. 2025, arXiv:2502.05048
Li, J., Silverman, J. D., Shen, Y., et al. 2025, ApJ, 981, 19
Li, J. I. H., Shen, Y., Ho, L. C., et al. 2021, ApJ, 906, 103
Li, J. I. H., Shen, Y., Ho, L. C., et al. 2023, ApJ, 954, 173
Lilly, S. J., Le Fèvre, Fè, Renzini, A., et al. 2007, ApJS, 172, 70
Liske, J., Baldry, I. K., Driver, S. P., et al. 2015, MNRAS, 452, 2087
Luo, B., Brandt, W. N., Xue, Y. Q., et al. 2017, ApJS, 228, 2
Lutz, D., Mainieri, V., Rafferty, D., et al. 2010, ApJ, 712, 1287
Lyke, B. W., Higley, A. N., McLane, J. N., et al. 2020, ApJS, 250, 8
MacLeod, C. L., Ivezić, Ž., Kochanek, C. S., et al. 2010, ApJ, 721, 1014
Magorrian, J., Tremaine, S., Richstone, D., et al. 1998, AJ, 115, 2285
Maiolino, R., Scholtz, J., Curtis-Lake, E., et al. 2024, A&A, 691, A145
Mallery, R. P., Mobasher, B., Capak, P., et al. 2012, ApJ, 760, 128
Mao, M. Y., Sharp, R., Norris, R. P., et al. 2012, MNRAS, 426, 3334
McAlpine, S., Bower, R. G., Harrison, C. M., et al. 2017, MNRAS, 468, 3395
Melchior, P., Moolekamp, F., Jerdee, M., et al. 2018, A&C, 24, 129
Menzel, M. L., Merloni, A., Georgakakis, A., et al. 2016, MNRAS, 457, 110
Merloni, A., Bongiorno, A., Bolzonella, M., et al. 2010, ApJ, 708, 137
Mezcua, M., Pacucci, F., Suh, H., Siudek, M., & Natarajan, P. 2024, ApJL, 966, L30
Mezcua, M., Siudek, M., Suh, H., et al. 2023, ApJL, 943, L5
Mountrichas, G. 2023, A&A, 672, A98
Mountrichas, G., Buat, V., Georgantopoulos, I., et al. 2021, A&A, 653, A70
Natarajan, P. 2011, arXiv:1105.4902
Natarajan, P., Pacucci, F., Ferrara, A., et al. 2017, ApJ, 838, 117
Natarajan, P., Pacucci, F., Ricarte, A., et al. 2024, ApJL, 960, L1
Noll, S., Burgarella, D., Giovannoli, E., et al. 2009, A&A, 507, 1793
Ochsenbein, F., Bauer, P., & Marcout, J. 2000, A&AS, 143, 23
Oliver, S., Rowan-Robinson, M., Alexander, D. M., et al. 2000, MNRAS, 316, 749
Pacucci, F., & Loeb, A. 2024, ApJ, 964, 154
Pacucci, F., Nguyen, B., Carniani, S., Maiolino, R., & Fan, X. 2023, ApJL, 957, L3
Pâris, I., Petitjean, P., Aubourg, É., et al. 2018, A&A, 613, A51
Ramos Padilla, A. F., Wang, L., Małek, K., Efstathiou, A., & Yang, G. 2022, MNRAS, 510, 687
Reines, A. E., & Volonteri, M. 2015, ApJ, 813, 82
Ren, W., Guo, H., Shen, Y., et al. 2024, ApJ, 974, 153
Ricarte, A., & Natarajan, P. 2018, MNRAS, 481, 3278
Sacchi, N., La Franca, F., Feruglio, C., et al. 2009, ApJ, 703, 1778
Scodeggio, M., Guzzo, L., Garilli, B., et al. 2018, A&A, 609, A84
Shankar, F., Bernardi, M., Richardson, K., et al. 2019, MNRAS, 485, 1278
Shaw, M. S., Romani, R. W., Cotter, G., et al. 2012, ApJ, 748, 49
Shen, Y., Hall, P. B., Horne, K., et al. 2019, ApJS, 241, 34
Shen, Y., & Kelly, B. C. 2010, ApJ, 713, 41
Shen, Y., & Liu, X. 2012, ApJ, 753, 125
Shen, Y., Richards, G. T., Strauss, M. A., et al. 2011, ApJS, 194, 45
Silverman, J. D., Mainieri, V., Salvato, M., et al. 2010, ApJS, 191, 124
Spitzer Science Center & Infrared Science Archive 2021, yCat, II, 368
Stalevski, M., Fritz, J., Baes, M., Nakos, T., & Popović, L. Č. 2012, MNRAS, 420, 2756
Stalevski, M., Ricci, C., Ueda, Y., et al. 2016, MNRAS, 458, 2288
Steffen, A. T., Strateva, I., Brandt, W. N., et al. 2006, AJ, 131, 2826
Stone, M. A., Lyu, J., Rieke, G. H., Alberts, S., & Hainline, K. N. 2024, ApJ, 964, 90
Suberlak, K. L., Ivezić, Ž., & MacLeod, C. 2021, ApJ, 907, 96
Suh, H., Civano, F., Trakhtenbrot, B., et al. 2020, ApJ, 889, 32
Suh, H., Hasinger, G., Steinhardt, C., Silverman, J. D., & Schramm, M. 2015, ApJ, 815, 129
Sun, Y., Lyu, J., Rieke, G. H., et al. 2024, ApJ, 978, 98
Tanaka, T. S., Silverman, J. D., Ding, X., et al. 2025, ApJ, 979, 215
Tie, S. S., Martini, P., Mudd, D., et al. 2017, AJ, 153, 107
Übler, H., Maiolino, R., Curtis-Lake, E., et al. 2023, A&A, 677, A145
van den Bosch, R. C. E. 2016, ApJ, 831, 134
Vestergaard, M., & Peterson, B. M. 2006, ApJ, 641, 689
Vestergaard, M., & Wilkes, B. J. 2001, ApJS, 134, 1
Villforth, C., Sarajedini, V., & Koekemoer, A. 2012, MNRAS, 426, 360
Vincenzi, M., Brout, D., Armstrong, P., et al. 2024, ApJ, 975, 86
Volonteri, M., & Natarajan, P. 2009, MNRAS, 400, 1911
Ward, C., Gezari, S., Nugent, P., et al. 2022, ApJ, 936, 104
Ward, C., Melchior, P., Sampson, M., et al. 2025, A&C, 51, 100930
Webb, N. A., Coriat, M., Traulsen, I., et al. 2020, A&A, 641, A136
Wenger, M., Ochsenbein, F., Egret, D., et al. 2000, A&AS, 143, 9
Wu, Q., & Shen, Y. 2022, ApJS, 263, 42
Wyithe, J. S. B., & Loeb, A. 2003, ApJ, 595, 614
Xia, L., Malhotra, S., Rhoads, J., et al. 2011, AJ, 141, 64
Yang, G., Boquien, M., Brandt, W. N., et al. 2022, ApJ, 927, 192
Yang, G., Boquien, M., Buat, V., et al. 2020, MNRAS, 491, 740
Yang, Q., Wu, X.-B., Fan, X., et al. 2017, AJ, 154, 269
Zhang, Y., Ouchi, M., Gebhardt, K., et al. 2023, ApJ, 948, 103
Zhuang, M.-Y., & Ho, L. C. 2023, NatAs, 7, 1376
Zhuang, M.-Y., Li, J., & Shen, Y. 2024, ApJ, 962, 93
Zhuang, M.-Y., Yang, Q., Shen, Y., et al. 2024, ApJS, 274, 42
Zou, F., Brandt, W. N., Chen, C.-T., et al. 2022, ApJS, 262, 15
Zou, F., Brandt, W. N., Ni, Q., et al. 2023, ApJ, 950, 136